Article

Dynamic Failure Mechanism and Fractal Features of Fractured Rocks Under Quasi-Triaxial Static Pressures and Repeated Impact Loading

Peng Li [1,2], Yan Liu [1], Jie Zhang [3,*], Zhihong Dong [1], Xinghui Wu [4], Shengjun Miao [1] and Meifeng Cai [1]

[1] Key Laboratory of Ministry of Education for Efficient Mining and Safety of Metal Mines, University of Science and Technology Beijing, Beijing 100083, China; pengli@ustb.edu.cn (P.L.)
[2] State Key Laboratory of Coal Resources and Safe Mining, China University of Mining and Technology, Xuzhou 221116, China
[3] China Enfi Engineering Corporation, Beijing 100089, China
[4] School of City and Architecture Engineering, Zaozhuang University, Zaozhuang 277160, China
[*] Correspondence: zhangjie.01@enfi.com.cn

Abstract: Mastering the dynamic mechanical behaviors of pre-stressed fractured rocks under repeated impact loads is crucial for safety management in rock engineering. To achieve this, repeated impact loading experiments were performed on produced fractured samples exposed to varying pre-applied axial and confining pressures using a split Hopkinson pressure bar test system in combination with a nuclear magnetic resonance imaging system, and the dynamic failure mechanism and fractal features were investigated. The results indicate that the dynamic stress–strain curves exemplify typical class II curves, and the strain rebound progressively diminishes with growing impact times. The impact times, axial pressure, and confining pressure all significantly affect the dynamic peak strength, average dynamic strength, dynamic deformation modulus, average dynamic deformation modulus, maximum strain, and impact resistance performance. Moreover, under low confining pressures, numerous shear cracks and tensile cracks develop, which are interconnected and converge to form large-scale macroscopic fracture surfaces. In contrast, specimens under a high confining pressure primarily experience tensile failure, accompanied by localized small-scale shear failure. Under low axial pressure, some shear cracks and tensile cracks emerge, while at high axial pressure, anti-wing cracks and secondary coplanar cracks occur, characterized predominantly by shear failure. In addition, as the confining pressure grows from 8 to 20 MPa, the fractal dimensions are 2.44, 2.32, 2.23, and 2.12, respectively. When the axial pressures are 8, 14, and 20 MPa, the fractal dimensions are 2.44, 2.46, and 2.52, respectively. Overall, the degree of fragmentation of the sample decreases with growing confining pressure and grows with rising axial pressure.

Keywords: fractured rock; dynamic mechanical properties; failure mechanism; fractal features; quasi-triaxial static pressure; repeated impact loading

1. Introduction

Due to various geological processes such as tectonic movements, volcanic activity, weathering, and erosion, rock masses in the crust produce various scales of randomly distributed defects (discontinuities), including microcracks, fissures, pores, joints, and faults [1–3] (Figure 1a), becoming a typical heterogeneous, discontinuous, and anisotropic geological material with extremely complex physical and mechanical features. The density

and spatial distribution of these discontinuous defects significantly alter the stress distribution pattern in the surrounding rock, thus considerably impacting the strength and fracture modes of the rock mass. Numerous studies [4–8] have indicated that under external loads, the original defects in rock masses are irreversibly deformed, and new cracks mainly occur and propagate at the boundaries (or tips) of these defects, causing nonlinear degradation of the mechanical parameters of the rocks and leading to the deformation and failure of the rocks and induced disasters. Defects greatly increase the complexity and unpredictability of rock mechanical behaviors [9], making it difficult to accurately predict the deformation and failure modes of the surrounding rocks in rock engineering, thereby increasing the risk of engineering disasters. Thus, it is crucial to discuss the mechanical features and failure mechanisms of rocks containing defects.
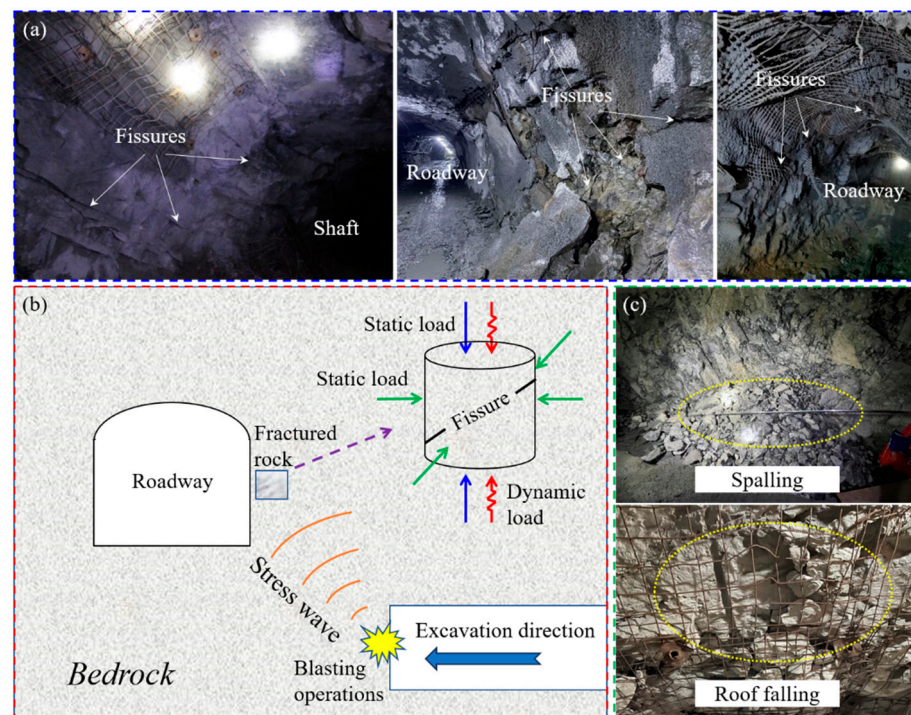

Figure 1. Complicated fissure structures distributed in subsurface rock projects (**a**), a schematic diagram of fractured rocks under combined dynamic and static stresses (**b**), and typical dynamic disasters that occurred in some underground excavations (**c**).

In subsurface rock engineering construction, the surrounding rock not only carries quasi-static stress (two-dimensional or three-dimensional) but is also often disturbed by various repeated dynamic loads such as frequent blasting operations, mechanical vibrations, and excavation construction [10–13] (Figure 1b), which promote fatigue damage to the rocks and pose a potential threat to rock stability. In the dynamic and static superposition mechanical environment, the elastic brittleness and compactness of the surrounding rock are enhanced, which is beneficial to the accumulation of elastic strain energy and the rapid and remote propagation of dynamic stress waves. Also, when stress waves propagate through the defects in the rock mass, they are reflected and scattered, which results in a sharp rise in local stress levels in a short time and a high concentration of dynamic stress. This can easily induce dynamic disasters such as rock bursts, collapse, roof falling, and spalling [14–17] (Figure 1c). Therefore, the study of rock damage characteristics and disaster mechanisms under the superposition of dynamic and static forces has become a hot topic in the field of engineering dynamic disaster prevention and control and safety management. Understanding the dynamic mechanical responses and rupture mechanism of

fractured rocks exposed to repeated impact loads is an important prerequisite for preventing and solving these problems, and it is of great significance for stability analysis, blasting technology design, and support structure optimization in rock engineering.

In recent years, a significant amount of effort has been devoted to exploring the dynamic mechanical behavior of fractured rocks using theoretical analysis, experiments, and numerical simulations. For instance, Zhao et al. [18] explored the influence of parallel joints on the transmission features of stress waves using the displacement discontinuity method. Li et al. [19] believed that the presence of prefabricated flaws may change the rupture pattern of rocks under dynamic loads, shifting from splitting-dominated by intact rocks to shear-dominated by rocks with joints. Wang et al. [20] investigated the dynamic mechanical response, crack propagation process, and energy evolution of fractured rocks under dynamic loading. You et al. [21] carried out triaxial dynamic tests on sandstone specimens containing multiple parallel flaws and found that as the joint strength increased, the failure mode of the fractured rocks shifted from shear-dominated to shear–tensile mixed failure. Shi et al. [22] claimed that existing fissures aligned with the impact direction provided stronger resistance compared with fissures that deviated from that direction, and the location and distribution of fissures significantly affected the impact stress transmission. Li et al. [12,23] conducted impact loading tests on parallel-fractured and cross-fractured granite samples containing holes to analyze the influences of fissure geometry and dynamic strain rate on the dynamic mechanical properties and cracking process of fractured rocks. Qiu et al. [24] simulated the effect of flaws' geometric parameters on the dynamic response and fracture behavior of jointed rocks. Chen et al. [25] studied the dynamic mechanical responses, energy evolution, and rupture patterns of jointed granite specimens. Previous studies have made important contributions to the understanding of the deformation, strength, initiation and propagation of cracks and the cracking modes of fractured rocks subjected to impact loading. However, these works were carried out under a single impact, ignoring the cumulative effect of cyclic dynamic pressures on the damage to fractured rocks.

In terms of cyclic impact loading tests, most scholars have examined the dynamic mechanical responses of intact rocks exposed to repeated impact pressures. For instance, Jiang et al. [26] noted that under repeated dynamic impacts, the porosity and permeability of rock progressively decreased, which primarily resulted from an overall reduction in pore size and the loss of pore connectivity. Wang et al. [27] reported that as the number of impacts grows, the dynamic strength and deformation capacity of rocks gradually drop, and fatigue damage gradually accumulates. Jiang et al. [28] stated that with increasing dynamic impact times, the porosity and permeability of red sandstone increase, and microcracks merge and propagate, ultimately forming larger microcrack areas. Lu et al. [29] suggested that the dynamic peak strength of sandstone descends with increasing impact times, and brittle failure occurs. Furthermore, the dynamic mechanical features of pre-applied intact rocks under repeated impact disturbance have also received some attention. Wang et al. [30] performed dynamic loading tests on red sandstone samples with confining pressure and studied the relationship between cyclic impact, dynamic characteristics, and porosity changes. Xue et al. [31] concluded that under the same pre-applied axial load, as the impact times increase, the peak strength of the rock shows a tendency of first growing and then descending. The above studies only emphasized the influence of cyclic dynamic impact on intact rocks. However, less attention has been focused on the mechanical behaviors and fracture characteristics of pre-stressed fractured rocks exposed to repeated impact loads. Zhang et al. [32] thought that under constant-cyclic impact pressure, the dynamic deformation modulus and strength of fractured rocks pre-loaded with axial compression first grow and then descend with an increasing joint angle. Luo et al. [33]

conducted dynamic triaxial cyclic impact experiments on coal rocks with different bedding angles, analyzing the effects of bedding and confining pressure on the dynamic mechanical features and damage and rupture laws of the coal rocks. Hence, the research on the dynamic mechanical features and cracking modes of fractured rocks under the combined action of quasi-triaxial static loads and cyclic dynamic loads is still insufficient; particularly, the dynamic failure mechanism and stability of fractured rocks are not fully understood, and further in-depth investigation is needed.

To address these issues, in this article, cylindrical granite specimens with prefabricated intermittent fissures were prepared, and repeated impact loading experiments on the produced fractured specimens under different pre-applied axial loads (8, 14, and 20 MPa) and confining pressures (8, 12, 16, and 20 MPa) were performed using a split Hopkinson pressure bar test system. Moreover, a nuclear magnetic resonance imaging system was employed to measure and identify the porosity and images of the fractured specimens after testing to analyze their dynamic damage behaviors. The stress wave fluctuation features, dynamic mechanical properties, fracture behaviors, and failure patterns of the fractured specimens subjected to varying axial and confining loads and the same repeated impact pressure were systematically examined. Accordingly, the dynamic failure mechanism of the fractured specimens was discussed. In addition, the distribution characteristics of the fragments and debris of the fractured specimens after testing were analyzed from the perspective of fragment size and mass, and the effect of different confining and axial pressures on the fractal dimension of the fractured specimens was also explored. The achieved results provide a new perspective for the surrounding rock stability evaluation, disaster prevention, and safety management of rock engineering.

2. Experimental Methodology

2.1. Specimen Preparation

The rock material employed in the experiment was medium-fine monzonitic granite taken from the Inner Mongolia region, China, and the same large block of rock with good geometric integrity and lithofacies uniformity was selected to prepare standard cylindrical samples with a size of 50 mm (diameter) × 100 mm (height) to reach a better comparison. The average density, longitudinal wave velocity, elastic modulus, Poisson's ratio, and porosity of the intact granite are approximately 2670 kg/cm^3, 3590 m/s, 38.54 GPa, 0.26, and 0.18%, respectively. Overall, the granite material has a dense texture, no visible cracks, and low porosity. Firstly, intact standard cylindrical samples were produced by the saw-cutting method, which causes less physical damage to specimens and the remaining rocks. Afterward, two symmetrical and coplanar prefabricated semi-elliptical fissures were created on both sides of the intact sample using high-pressure water jet technology. After inspection, the processing quality was quite good, and no additional damage was caused to the sample. The geometry of the specimen configuration designed for the experiment is described in Figure 2. The fissure width was 0.3 mm, the fissure length *c* was 16.35 mm, and the fissure angle β, i.e., the included angle between the plane where the fissures on both sides of the specimen are located and the horizontal plane (perpendicular to the impact loading orientation), was 45°. Note that the selected fissure angle and length were respectively derived from the investigation results of the dominant occurrence and continuity of structural planes in a metal mine roadway, which were simulated similarly on the sample. To deliberate on the effect of axial compression and confining pressure on the dynamic mechanical response behavior of fractured rocks, six groups of specimens, each with three specimens, were prepared and tested. Photographs of the processed fractured specimens for testing are given in Figure 3. Note that prior to the mechanical testing, density and wave velocity tests were conducted on three specimens in each group, and the detection

results were in good agreement. The loading ends of each specimen were carefully polished to guarantee that the non-parallelism and non-perpendicularity errors were smaller than 0.02 mm [3], thereby preventing the stress concentration of rock samples caused by eccentric pressure during repeated impact loading from affecting the experimental results. After the testing, a typical specimen was selected from each group for a detailed study [7,34].
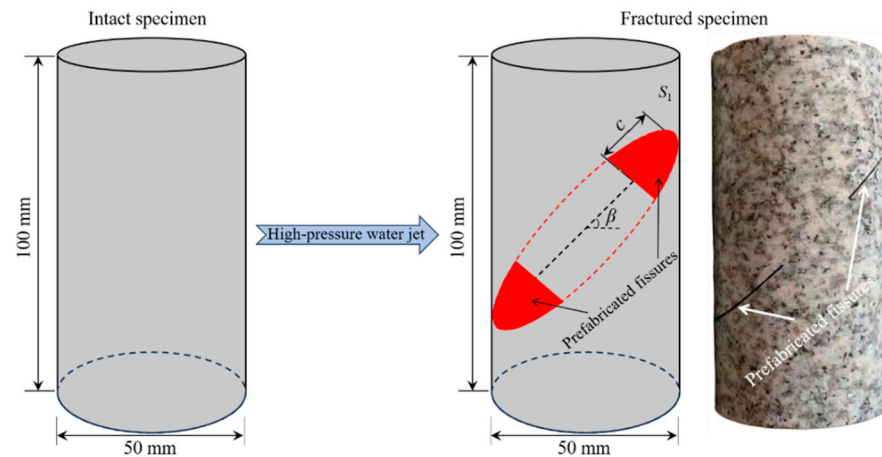

Figure 2. Illustration of the geometry configurations of the designed samples.

Figure 3. Photographs of the processed fractured specimens for testing.

2.2. Testing Devices

2.2.1. Split Hopkinson Pressure Bar System

The split Hopkinson pressure bar (SHPB) system has been widely adopted to study the dynamic mechanical behavior of rock materials at medium to high strain rates (10^2–10^4 s^{-1}). In this experiment, the SHPB device was used to conduct repeated impact loading experiments under different quasi-triaxial confining pressures on the fractured specimens produced. The photographic and schematic diagrams of the SHPB system are illustrated in Figure 4a and Figure 4b, respectively. This system mainly consists of an impact loading device, a measuring device, and a data acquisition and processing device. The impact loading device primarily involves a high-pressure cylinder, a cone-shaped striker, an incident bar, a transmitted bar, an absorption bar, a confining pressure device, and an axial pressure device. The improved cone-shaped striker and the cylindrical incident, transmitted, and absorption bars are all made of the same high-strength steel material, with a longitudinal wave velocity of 5447 m/s, elastic modulus of 240 GPa, and uniaxial compressive strength of 800 MPa. The length of the cone-shaped striker is 360.1 mm, the lengths of the incident and transmitted bars are 1800 mm, and the length of the absorption bar is 1000 mm. The

centers of the three bars are aligned, and their cross-sectional areas (the diameter is 50 mm) are the same.
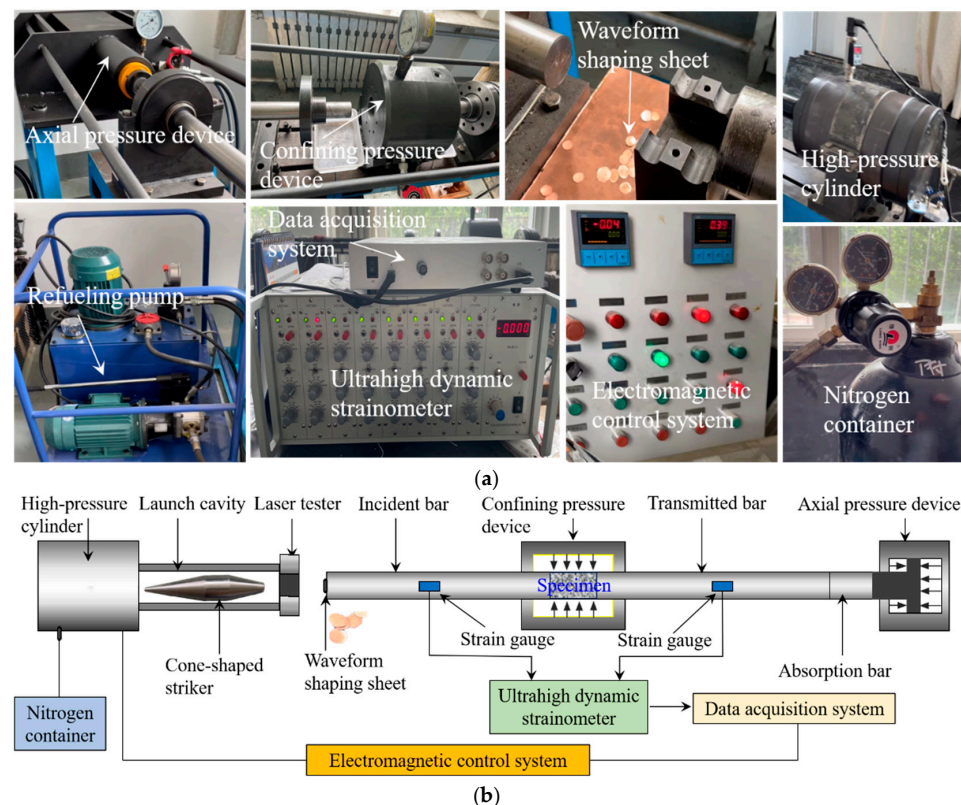

Figure 4. Photographic (**a**) and schematic (**b**) diagrams of the SHPB system.

The SHPB device can generate one-dimensional stress pulses by the cone-shaped striker placed in the launching cavity concentrically impacting the incident bar, and the stress pulses diffuse towards the interface between the incident bar and the specimen at a certain wave speed. The amplitude of the loading waveform can be governed by regulating the impact speed of the cone-shaped striker. The improved cone-shaped striker can form a half-sine wave to obviate high-frequency oscillations, diminish dispersion effects, prevent uneven stress, and ensure a constant strain rate loading [23,35]. Furthermore, when the cone-shaped striker collides with the incident bar, a waveform shaping sheet is put in place to further reduce the dispersion effect of the stress wave. After the stress wave is repeatedly reflected and transmitted in the specimen several times, the stress at both ends of the sample appears to balance. Throughout the experiment, the strain signals of the incident wave, reflected wave, and transmitted wave were collected in real-time and continuously using the BE120-SAA strain gauges attached to the incident and transmitted bars, with a maximum acquisition frequency of 1000 kHz. Based on Kolsky's theory [36], the dynamic stress–strain behavior of the specimen can be calculated from the strain signals collected by the strain gauges.

2.2.2. Nuclear Magnetic Resonance Imaging System

The nuclear magnetic resonance imaging (NMRI) system uses an external gradient magnetic field to emit multi-frequency electromagnetic waves to distinguish between the attenuation of nuclear magnetic resonance signals in diverse structures inside materials. By analyzing the attenuation law of the signals, the position and type of the internal structure of the material can be determined, and then images of different structures inside the substances can be drawn accordingly. The MacroMR12-150H-I NMRI system was

adopted in this experiment, which mainly includes three parts, i.e., a testing system, a control system, and a matching ZYB-II vacuum pressurization saturation device (Nantong, China), as displayed in Figure 5. The magnetic field strength of the NMRI system is within the range of 0.25–0.35 T, the radio frequency transmission power is greater than 300 W, and the resonant frequency is 12.63 MHz. The maximum pressure of the vacuum pressurization saturation device is 60 MPa.
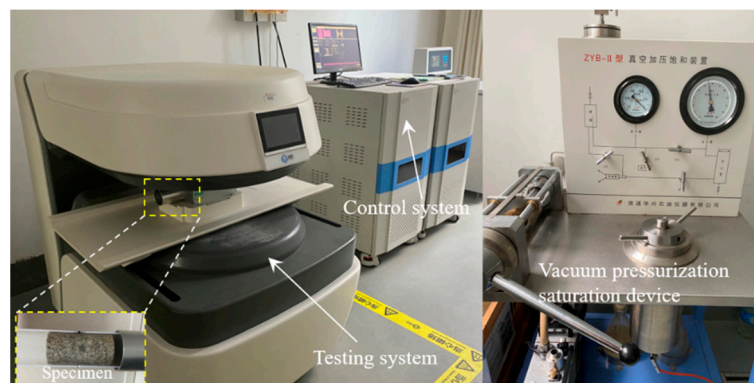

Figure 5. Photographic diagram of the NMRI system.

For rock materials, before conducting NMRI, the rock sample needs to be saturated with water to allow as many hydrogen nuclei as possible to converge on the pores and cracks inside the sample, so that the damage formed inside the sample can be reflected by the distribution of pore water. The more hydrogen nuclei in the sample, the larger the porosity. Hence, the rock porosity index can be employed to quantitatively characterize the damage of the tested sample. The porosity calculation formula is as follows:

$$P = (V_0/V) \times 100\% \tag{1}$$

where P is the porosity; V_0 represents the volume of pores and cracks in the sample; and V means the total volume of the sample.

2.3. Experimental Procedures

In the repeated impact loading test, the specimen was subjected to a certain pre-loaded axial pressure P_a and confining pressure P_c simultaneously. The specific experimental scheme for the repeated impact tests on the fractured sample under quasi-triaxial static pressures is shown in Table 1, and the loading methods for the quasi-triaxial static loads and stress wave loads are depicted in Figure 6. Under the designed axial and confining pressure conditions, the single impact load should fall within the dynamic damage threshold range of the fractured specimen to achieve repeated multiple impacts. Through multiple trial-and-error tests, it was determined that the impact pressure P_i for each test was 0.35 MPa (the corresponding impact velocity is 20.56 m/s). Under this impact pressure, the specimen will not experience severe fragmentation after at least 19 repeated impacts, while noticeable damage accumulation occurs. This makes it suitable for measuring the porosity and imaging of the specimen using the NMRI system, allowing for the analysis of the progressive dynamic damage behavior of the specimen.

The main experimental procedures were as follows. Firstly, the sample was placed into the confining pressure device and aligned with the central axis of the impact bars. Next, a hydraulic pump was used to sequentially apply confining pressure and axial pressure to the specimen at a rate of 0.5 MPa/s until they reached the design values and remained constant. Such a low loading rate can prevent specimen failure during the application of confining and axial pressures. Then, the specimen was repeatedly collided against with

the same impact pressure of 0.35 MPa. After several impacts, the sample failed and the test ended. During the tests, the experimental data were synchronously recorded and saved after each impact. Notably, prior to the experiment, the SHPB system was calibrated for an empty impact test to ensure that it met the general requirements (one-dimensional stress wave transmission and uniformity of stress and strain) of the impact test [23,35]. The confining pressure and axial pressure should be calibrated prior to each impact to guarantee consistency with the set values. Moreover, to achieve the consistency of the incident wave each time, the positions of the cone-shaped striker and the incident bar should be ensured to be the same before each impact test. In the experiment, the friction between the sample and bar can cause a waveform dispersion effect, which affects the accuracy of the test results. Hence, waveform shaping sheets were employed, along with a uniform application of lubricant to both ends of the sample, to minimize the waveform dispersion effect.

Table 1. Experimental scheme.

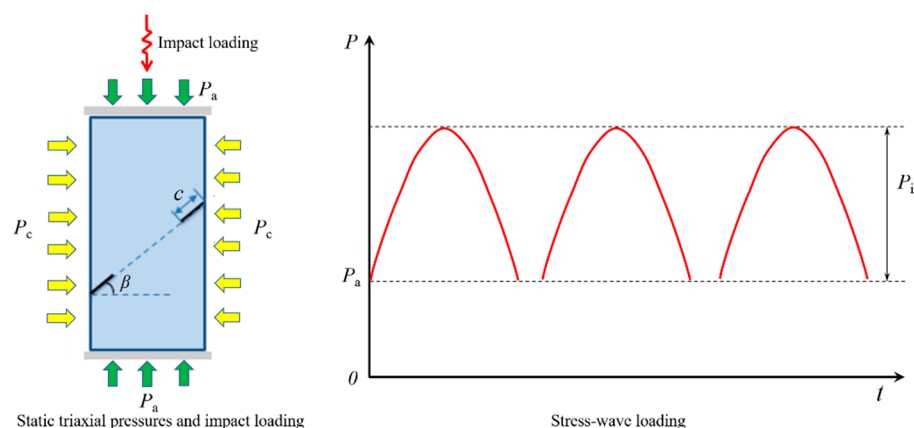| Sample Number	Axial Pressure/MPa	Confining Pressure/MPa
FGS-1	8	8
FGS-2	8	12
FGS-3	8	16
FGS-4	8	20
FGS-5	14	8
FGS-6	20	8

Figure 6. Loading methods for the quasi-triaxial static loads and stress wave loads.

It should be noted that after the experiments and inspection, the dynamic mechanical properties, fracture behavior, and fractal features of the three specimens within each group were quite similar and had good consistency. Thus, the analysis and discussion of the test results could focus on a typical specimen selected in each group [7,34,37,38], and the conclusions obtained were considered to be representative.

3. Dynamic Mechanical Properties

3.1. Stress Equilibrium Validation

In rock impact loading tests, due to the instantaneous nature of the impact load, the generated stress waves may lead to complex stress distributions inside the specimen, so stress equilibrium validation is a critical step in ensuring the accuracy and reliability of test results. An effective SHPB test must satisfy two essential assumptions: one-dimensional stress wave transmission and the uniformity of stress and strain. For fractured specimens, prefabricated fissures in the specimen may affect the spread of stress waves. Thus, before

analyzing the results of the impact tests, clarifying the validity of using the SHPB system to conduct impact loading experiments on the fractured specimens is necessary. In the SHPB tests, the dynamic stress balance between the two ends of the specimen should be achieved prior to the specimen rupture, particularly prior to peak stress occurring in the specimen. This can be checked by comparing the dynamic stress histories at both ends of the samples. In this study, the use of a cone-shaped striker to generate a slowly rising one-dimensional half-sine wave on the compression bar, as well as the use of waveform shaping sheets and the uniform application of lubricant to both ends of the sample to diminish end-face friction, are beneficial measures for significantly eliminating stress wave oscillations and reducing wave dispersion effects. This enables a uniform strain rate loading and dynamic stress balance at the specimen ends. Additionally, according to relevant studies [39,40], stress waves must travel back and forth through the sample at least three times to facilitate a dynamic stress balance. According to the relevant calculation formula [23], it takes approximately 50 μs for the stress wave to propagate back and forth in the specimen once, and the duration of the incident wave is around 240 μs in the experiments, which is enough for the stress wave to propagate back and forth in the sample at least four times to reach the stress balance.

Currently, a widely accepted approach for assessing dynamic stress equilibrium is to compare the transmitted wave with the superposition wave (i.e., the sum of the incident and reflected waves). The collected typical voltage signals of the incident, reflected, and transmitted waves (Figure 7a) of the representative specimen FGS-4 under the impact loading are converted, yielding the stress equilibrium relationship, as plotted in Figure 7b. According to the degree of overlap between the transmitted wave and the superposition wave in the stress equilibrium relationship, it can be determined whether the stress equilibrium condition is satisfied. In Figure 7b, the typical stress history at both ends of sample FGS-4 indicates that after multiple reflections, the superposition wave roughly overlaps with the transmitted wave before the specimen failure and remains in the post-peak region for a certain period. This means that the designed fractured specimen can reach a basic stress balance state during impact loading, demonstrating the availability and reliability of our SHPB tests. It should be noted that the same conclusion was also reached from the inspection of the other fractured specimens tested. In fact, many scholars [41–43] have conducted impact loading experiments on rocks containing defects (such as fissures and cavities) and obtained satisfactory results. Accordingly, based on the collected incident, reflected, and transmitted strain signals, the axial stress $\sigma(t)$, strain $\varepsilon(t)$, and strain rate $\dot{\varepsilon}(t)$ of the fractured specimens can be approximately computed by the relevant formulas in the one-dimensional stress wave propagation theory, namely:

$$\sigma(t) = \frac{A_e E_e}{2A_s}[\varepsilon_I(t) + \varepsilon_R(t) + \varepsilon_T(t)] \tag{2}$$

$$\varepsilon(t) = \frac{c_0}{l_s}\int_0^t [-\varepsilon_I(t) + \varepsilon_R(t) + \varepsilon_T(t)]dt \tag{3}$$

$$\dot{\varepsilon}(t) = \frac{c_0}{l_s}[-\varepsilon_I(t) + \varepsilon_R(t) + \varepsilon_T(t)] \tag{4}$$

where A_e and E_e represent the cross-sectional area and elastic modulus of the compression bar, respectively; A_s and l_s stand for the cross-sectional area and length of the specimen, respectively; $\varepsilon_I(t)$, $\varepsilon_R(t)$, and $\varepsilon_T(t)$ denote incident, reflected, and transmitted strain signals, respectively; and c_0 means the longitudinal wave velocity of the compression bar.
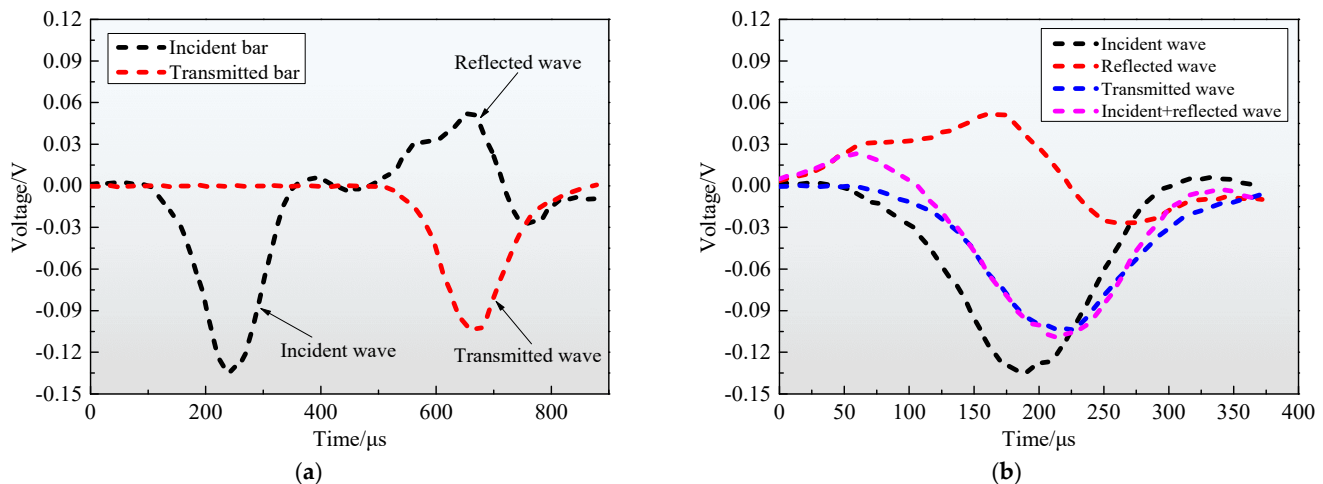
Figure 7. Typical voltage signals of the incident, reflected, and transmitted waves (**a**) and the examination of stress equilibrium (**b**).

3.2. Stress Wave Characteristics

The spread characteristics of stress waves inside the rocks during impact loading significantly affect the dynamic responses and failure patterns of the rocks. When stress waves propagate to structural planes, fissures, or discontinuities in rock masses, they can cause the initiation, growth, and connection of cracks, ultimately resulting in rock mass rupture. The reflected wave can reflect the strain changes, and the transmitted wave can characterize the average stress changes in the rock mass. Thus, understanding the transmission features of stress waves can help to better predict the dynamic mechanical features and failure mechanisms of rocks. Figure 8 shows the three-wave voltage versus time curves of the fractured specimens under different quasi-triaxial pressures and repeated impact loading. Because of the high number of repeated impact times in the experiment, only partial curves of each sample are presented. Under the same impact pressure, the amplitude of the incident wave basically overlaps, and the incident, reflected, and transmitted waves are all half-sine waves. The incident waves of multiple impacts have a good coincidence, suggesting that the impact velocity has been precisely controlled. When stress waves are loaded on the specimen, the filtered incident waveform will not exhibit significant oscillations. The amplitude of the transmitted wave is less than that of the incident wave, and the variation trend of the reflected wave is generally opposite to that of the transmitted wave. These specimens have similar stress wave features. The pre-existing fissures in the specimen have a certain effect on the transmission of stress waves in the specimen, leading to varying degrees of fluctuations in the stress waves. This may be because, under one-dimensional stress wave conditions, fissures undergo varying degrees of inelastic deformation, which makes the stress waves jump to different degrees.

On the other hand, under constant impact pressure, the amplitude of the incident wave is the same, while the reflected wave and transmitted wave have approximately coincident waveforms in the first few impacts, suggesting that the impact triggered a slight damage to the rock in the stage before the formation of micropores and cracks. The amplitude of the transmitted wave reaches its maximum value in the first impact and decreases in subsequent impacts. Under the same impact pressure, the degree of damage to the rocks varies. In the early stages, the transmitted wave amplitude of rocks is small, and the energy consumption is low. After multiple repeated impacts, the damage accumulates and forms microcracks, increasing the energy consumption of the rock damage. With increasing impact times, the energy consumption of the sample damage also increases gradually.
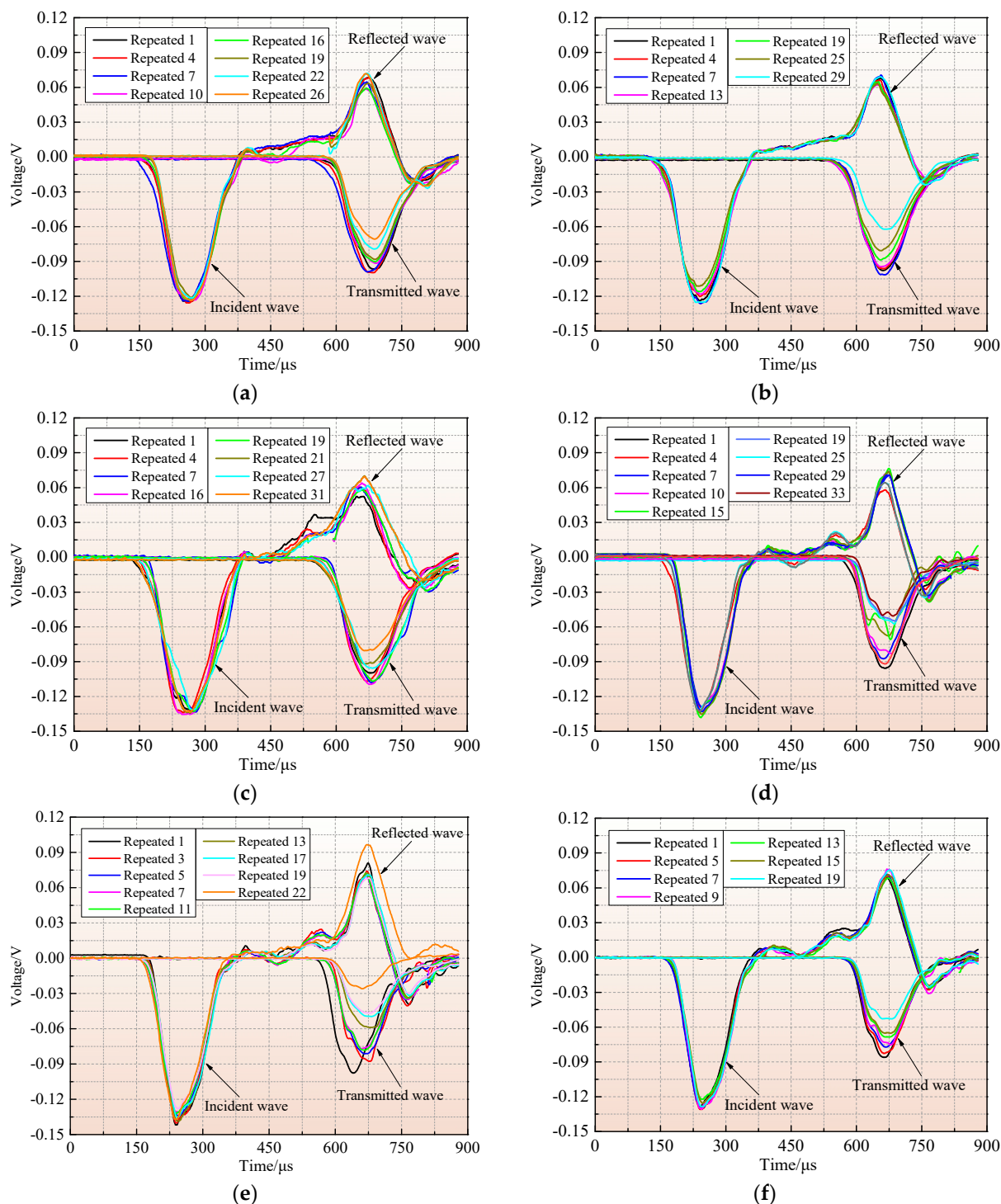
Figure 8. Typical three-wave voltage–time curves of the fractured specimens exposed to different quasi-triaxial pressures and repeated impact loading: (**a**) specimen FGS-1; (**b**) specimen FGS-2; (**c**) specimen FGS-3; (**d**) specimen FGS-4; (**e**) specimen FGS-5; (**f**) specimen FGS-6.

In addition, as the impact times increase, the amplitude of the transmitted wave progressively decreases, indicating that the degree of damage of the specimen increases during the cyclic impact process. With the initiation and growth of new cracks inside the sample, the number of reflections of the incident wave on the crack surface increases, which results in a fall in the transmitted energy produced by the incident wave after passing through the sample, and thus the corresponding amplitude of the transmitted wave is weakened. The amplitude of the reflected wave of the sample appears to increase at the

last impact, which may be because, after the sample is damaged under the impact load, the pre-loaded static pressures make the stress wave unable to transmit, resulting in an increase in the reflection of the stress wave at the end of the specimen, and therefore the corresponding amplitude of the reflected wave increases. When P_c = 8 MPa, the amplitude of the transmitted wave declines with increasing P_a values, and cracks develop in the specimen, and the damage progressively accumulates until the cracks propagate and penetrate. At this time, the ability of the specimen to resist external impacts weakens. Moreover, when the pre-loaded P_a is 8 MPa, the amplitude of the transmitted wave descends with a growing P_c value, indicating that increasing the P_c within a certain range can limit the initiation and growth of cracks in the sample, thereby enhancing the ability of the rock to resist external impacts.

3.3. Dynamic Stress–Strain Behavior

The representative dynamic stress–strain curves of the fractured samples exposed to diverse quasi-triaxial static pressures and repeated impact loading are presented in Figure 9. In general, the dynamic stress–strain behavior of the fractured specimens subjected to diverse stress conditions exhibits a certain degree of similarity. The curves of these samples have almost no noticeable initial compaction stage (concave curve) and directly enter the approximate elastic deformation stage after the specimens are subjected to impact loads. This is because the stress pulse duration is extremely short, and the initial micro-cracks cannot be closed in time under the impact load, resulting in the curve in the initial stage being almost linear, without a compaction process. Also, these curves are relatively smooth, without a significant stress drop. Similar phenomena have also been observed in some previous studies [12,19,44].

The dynamic stress–strain curves of the samples exposed to various P_c and P_a values can be roughly divided into three stages: the approximate elastic stage, crack propagation stage, and post-failure stage (i.e., the stage after peak stress). In the approximate elastic stage, the internal cracks of the sample are compacted, and the specimen maintains elastic deformation. As such, the dynamic stress–strain curve is nearly a straight line. At this stage, the load is largely borne by the particle skeleton and holes of the specimen. After multiple impacts, the sample still maintains good elastic deformation properties at this stage. In the crack expansion stage, with the increase in stress, some holes and cracks expand and penetrate, and the tangent slope of the stress–strain curve is smaller than that in the approximate elastic stage. At this stage, the loading stress exceeds the ultimate load of most holes, leading to the collapse of the holes. Near the collapsed holes, the stress rapidly concentrates, causing a temporary strain-hardening phenomenon. The stress–strain curve temporarily shows an upward convex form, and the tangent slope first increases and then decreases. Moreover, after multiple impacts, the tangent slope sharply decreases, and the stress–strain curves of several samples are nearly horizontal. The main reason for this is the formation of a large number of cracks in the specimens, forming a stress relaxation platform. In the post-failure stage, the stress generally declines with increasing strain, manifested as a typical class II rebound curve. The class II curve reveals the strain rebound phenomenon of the sample during the unloading process. At this time, the specimen has not completely broken and still has a certain bearing capacity. The reason for the rebound phenomenon is that the specimen initially has a high integrity and large wave impedance [45]. When stress waves are transmitted to the specimen, the larger wave impedance of the sample increases the amplitude of the transmitted wave. The larger the amplitude of the transmitted wave, the smaller the corresponding amplitude of the reflected wave, and the faster the time to reach the peak point. However, with the continuous action of the incident stress wave, the reflected wave amplitude begins to decrease, eventually

causing the direction of the reflected wave to be consistent with that of the incident wave, and the strain begins to descend, resulting in the strain rebound phenomenon. Another explanation is that during the pre-loading confining and axial pressures to the specimens, a certain amount of elastic energy is stored in the specimens, and the repeated impact loads do not cause the samples to completely break, resulting in the original elastic stress in the specimens being greater than the loading stress during stress unloading. The residual elastic strain energy accumulated in the sample is released during the unloading process, which leads to the rebound phenomenon.
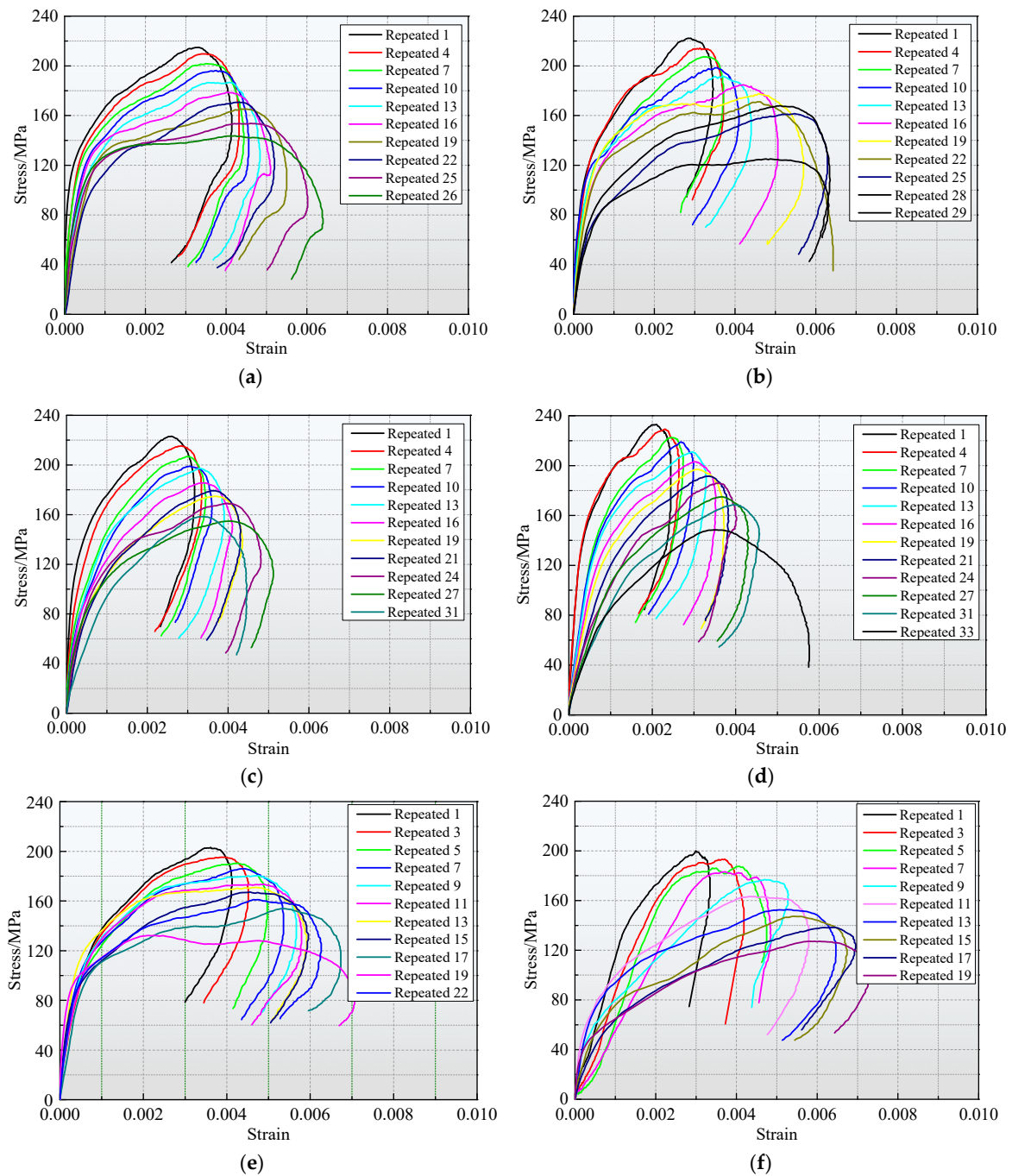
Figure 9. Dynamic stress–strain curves of the fractured specimens under different quasi-triaxial pressures and repeated impact loading: (**a**) P_a = 8 MPa, P_c = 8 MPa; (**b**) P_a = 8 MPa, P_c = 12 MPa; (**c**) P_a = 8 MPa, P_c = 16 MPa; (**d**) P_a = 8 MPa, P_c = 20 MPa; (**e**) P_a = 14 MPa, P_c = 8 MPa; (**f**) P_a = 20 MPa, P_c = 8 MPa.

According to the stress–strain curves after multiple impacts, with increasing impact times, the strain rebound phenomenon of the specimen gradually weakens. This is because microcracks in the specimen begin to expand and penetrate with increasing impact times, and the damage is aggravated, which leads to a decrease in the wave impedance of the specimen. As a consequence, when the stress wave is transmitted to the sample, the amplitude of the superimposed reflected wave grows and the amplitude of the transmitted wave declines due to multiple reflections at the crack interface. Additionally, the peak value of the reflected wave appears later because the direction of the reflected wave is opposite to that of the incident wave. At the same time, because the direction of the transmitted wave is consistent with that of the incident wave, the time of the transmitted wave peak appears earlier and earlier. According to the hypothesis of stress uniformity, the strain of the sample begins to increase, the stress decreases, and the rebound phenomenon gradually weakens. Under the final impact, the first half of the dynamic stress–strain curves of the samples remains approximately straight, while the second half has a significant right-leaning shape, the samples are broken, and the peak strains increase. For the same specimen, as the impact times increase, the hysteresis loop area of the specimen significantly increases.

The difference in the dynamic stress–strain curves of the samples exposed to varying P_c and P_a values is primarily manifested in the growth rate and plastic section. This may be due to the diverse matching correlations between the wave impedance of the specimen and the incident bar under different stress conditions, resulting in differences in the stress level of the specimens. The irreversible plastic deformation of the specimen after dynamic failure is relatively larger in two cases—when the P_a is constant and the P_c is smaller, and when the P_c is constant and the P_a is larger—which agrees fairly well with the expected results.

3.4. Dynamic Strength and Deformation Properties

3.4.1. Dynamic Strength Characteristics

The maximum stress corresponding to the dynamic stress–strain curve obtained for each impact in the repeated impact test of pre-stressed specimens is called the dynamic peak strength (DPS) of the fractured sample at that impact. Figure 10 reveals the variation in the DPS with the impact times. The impact times, P_a, and P_c all have significant effects on the DPS of the specimen. Under certain axial and confining pressures, the DPS of the specimen decreases linearly with increasing impact times. As P_a and P_c grow, the change in DPS presents a certain regularity. Specifically, in Figure 10a, when P_a = 8 MPa, as P_c increases from 8 to 20 MPa, the DPS shows an increasing trend, indicating that increasing the P_c value within the designed range increases the specimen's ability to resist impact disturbances. In Figure 10b, when P_c = 8 MPa, as P_a grows from 8 to 20 MPa, the DPS tends to decrease. That is, when the impact times are the same and the P_c remains unchanged, the DPS reduction rate of the rock is greater under larger axial pressure. In summary, the development of cracks inside rocks is influenced by both axial and confining pressures, and the stress environment in which the rock is located promotes corresponding changes in the structural characteristics of the rock, ultimately altering its mechanical properties.

The average value of the DPS of each impact obtained in the repeated impact test is defined as the average DPS of the sample. The correlation between average DPS and axial and confining pressures can indirectly reflect the influence of pre-loading on the deterioration of rock strength. Figure 11 displays the variation in the average DPS of the sample with a rising P_c and P_a. As presented in Figure 11a, the average DPS of the sample rises with increasing P_c values, which indicates that P_c significantly improves the compactness of the specimen. As the P_c value increases, the development of microcracks is inhibited, and the internal microcracks of the sample are tightly closed, resulting in a further increase in compactness. In Figure 11b, the average DPS tends to descend with

increasing P_a values, mainly because axial pressure facilitates the initiation and propagation of microcracks inside the specimen, which leads to a decline in the number of impacts the specimen can withstand under the same impact pressure and a decrease in its capability to resist external impact disturbances. If the difference between P_a and P_c is defined as deviatoric stress, it can be inferred that the smaller the deviatoric stress, the stronger the rock's capability to withstand external impacts.

(**a**) P_a = 8 MPa   (**b**) P_c = 8 MPa
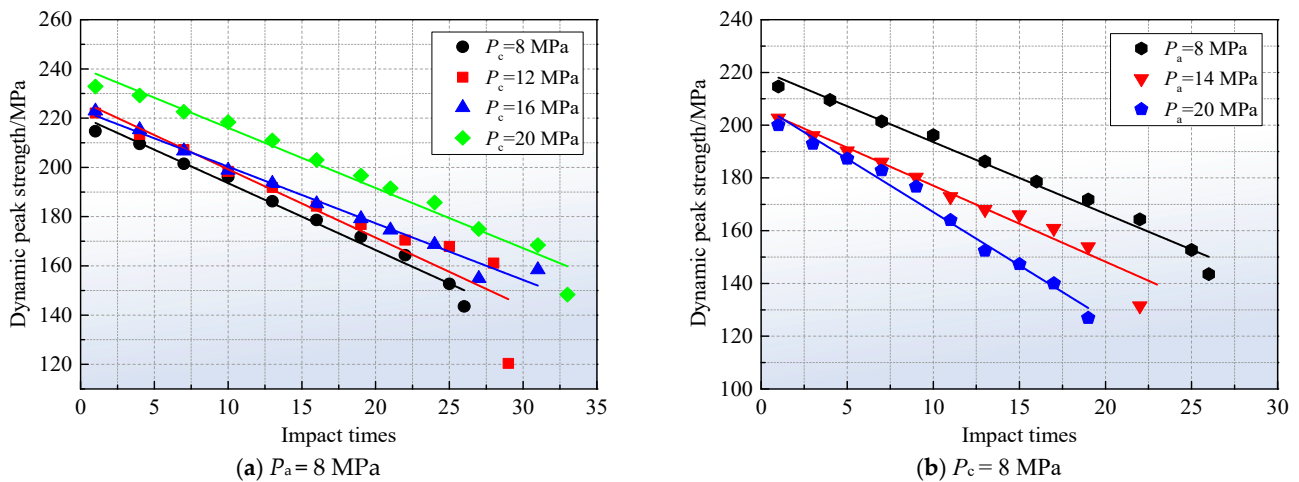
Figure 10. Variation in DPS with impact times when exposed to diverse P_c (**a**) and P_a (**b**) values.

(**a**) P_a=8 MPa   (**b**) P_c=8 MPa
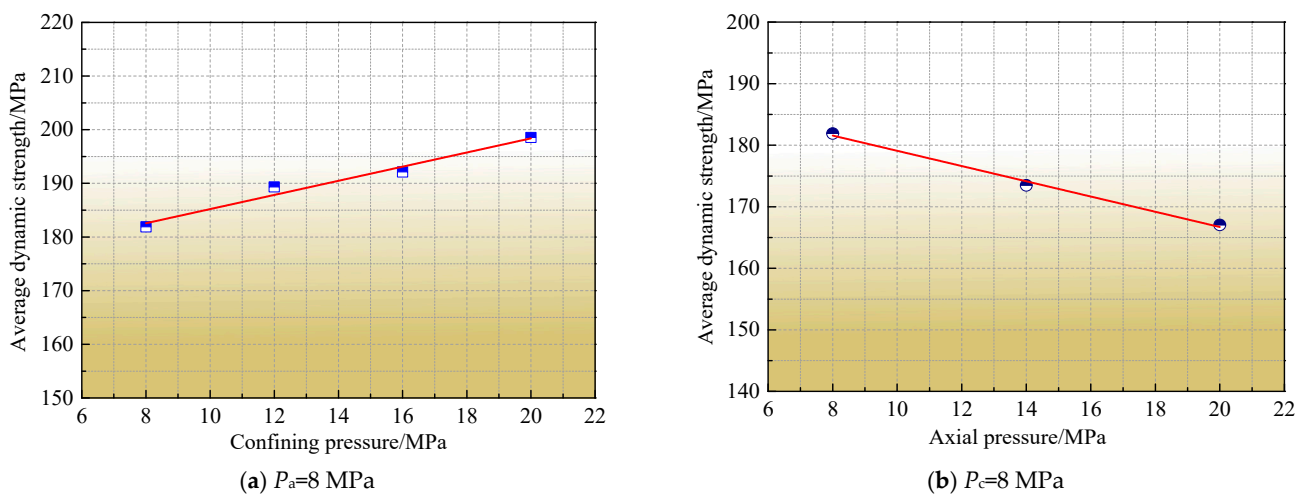
Figure 11. Variation in average DPS with confining pressure (**a**) and axial pressure (**b**).

3.4.2. Dynamic Deformation Characteristics

Under the action of dynamic impact loads, rocks undergo instantaneous deformation, and the elastic deformation of rocks in a very short time can be ignored. Hence, the dynamic deformation modulus (DDM) can more accurately reflect the dynamic deformation features of rocks. The DDM is defined as the weighted average of the secant modulus, the first type of secant modulus, and the deformation modulus of the loading section of the dynamic stress–strain curve [46]. The correlation between the DDM of the sample and the number of impacts is drawn in Figure 12. There are certain differences in the trend of the DDM with impact times under various P_a and P_c values. In Figure 12a, when P_a = 8 MPa and the P_c values are 8, 12, 16, and 20 MPa, the DDM shows a rapid downward tendency with increasing impact times. This is the result of the cumulative evolution of internal damage in the specimen during the cyclic impact process. As the number of impacts increases, the capability of the sample to resist external dynamic loads decreases, and the magnitude of

deformation also relatively increases under the same impact load. When the P_c values are 8 and 12 MPa, respectively, their DDM in the initial impact stage appears cross-phenomenon, that is, when P_c = 8 MPa, the DDM decreases slowly. When P_c = 16 MPa, there is an increase in deformation modulus at the last impact. Moreover, with increasing P_c values, the DDM rises, with the maximum DDM at a P_c value of 20 MPa and the minimum DDM at a P_c value of 8 MPa.
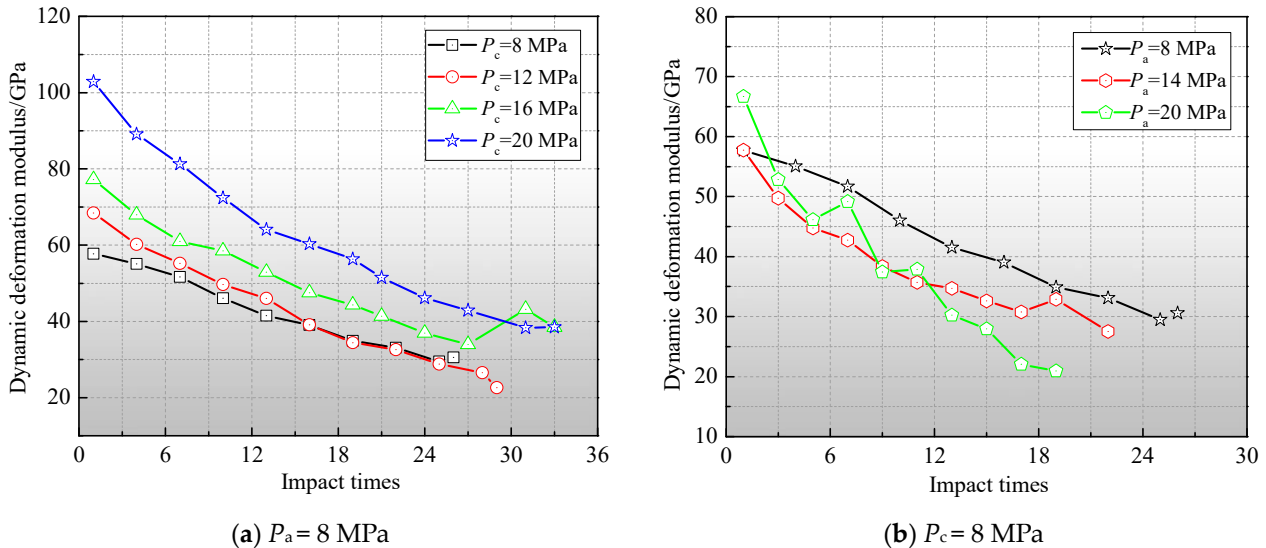

Figure 12. Variation in DDM with impact times under various P_c (**a**) and P_a (**b**) values.

In Figure 12b, when P_c = 8 MPa and the P_a values are 8, 14, and 20 MPa, the DDM also shows a downward trend with increasing impact times. The decrease in DDM during the first few impacts is significant. This is because the pre-loaded axial compression makes the microcracks inside the specimen almost completely closed, resulting in damage to the sample during the impact process. The impact resistance of the specimen is greatly reduced, but at this time, the original or newly generated microcracks in the specimen propagate very slowly or even have no time to propagate. In the subsequent repeated impact process, when P_a = 8 MPa, the DDM decreases almost uniformly. When P_a = 14 MPa, the DDM decreases uniformly at first and then suddenly. These phenomena can be attributed to the slow expansion of internal microcracks in the sample after multiple impacts. Because of the rapid impact rate, the time for microcrack expansion is limited, resulting in a period of uniform expansion. However, the cumulative damage progressively increases, and the impact resistance of the sample will continue to decrease. Finally, the sudden drop in the DDM is due to the penetration of microcracks, which promotes the macroscopic failure of the sample. When P_a = 20 MPa, the DDM decreases rapidly, and the magnitude of the decrease is also significant. This is because pre-applied axial pressure has already caused microscopic damage to the specimen, and the specimen experienced the compaction and slow propagation of internal microcracks when the axial pressure was pre-loaded. Under the action of impact load, the specimen begins to undergo macroscopic failure, and the DDM drops rapidly. This is also the reason why the total number of repeated impacts that the sample can withstand under higher axial pressure is lower. In addition, the DDM descends with increasing P_a values. When the P_a values are 14 and 20 MPa, their DDM exhibits a cross-phenomenon during the impact stage. The variability in the DDM of the sample under axial pressure conditions is greater than that under confining pressure conditions. The decreasing trend in the DDM varies with different P_a and P_c values, and the dynamic mechanical properties of rock masses exposed to diverse static stress environments may also differ significantly under the same impact disturbance. Therefore,

fully understanding the changing law of the rock DDM can provide a theoretical basis for predicting the dynamic failure of engineering rock masses.

The average DDM is calculated using the DDM of the samples after each impact under the same P_a value as well as the same P_c value. The correlation between the average DDM and the P_a and P_c values is shown in Figure 13. When P_a = 8 MPa, the average DDM of the specimen shows an increasing trend with increasing P_c values (Figure 13a). The presence of confining pressure prevents the lateral deformation of the specimen and enhances the rock's ability to resist external impacts to some extent. In Figure 13b, when P_c = 8 MPa, with increasing P_a values the average DDM drops, that is, the more new microcracks germinate inside the specimen under the same impact pressure, the greater its compression deformation.

(**a**) P_a = 8 MPa (**b**) P_c = 8 MPa
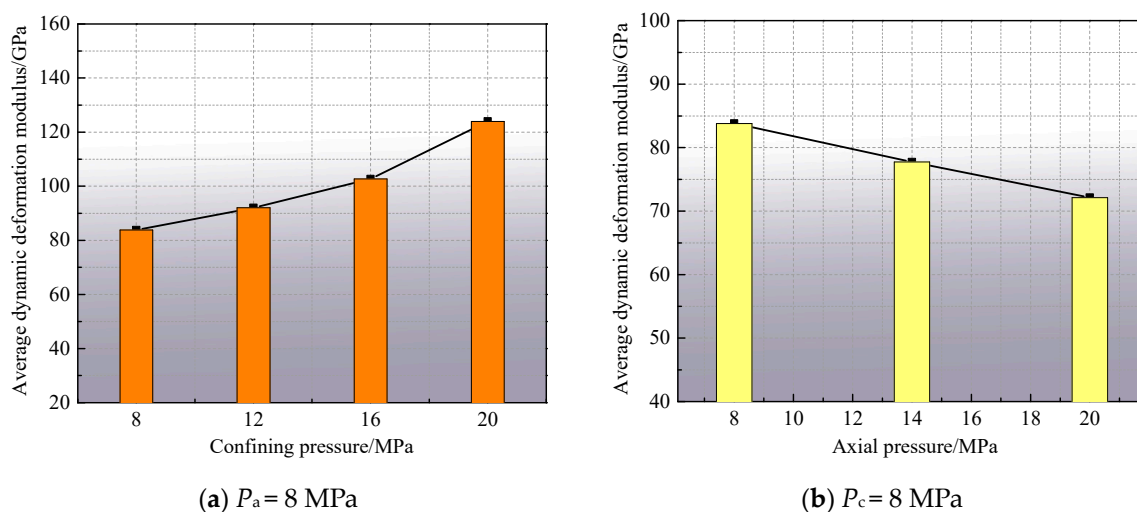
Figure 13. Variation in average DDM with confining pressure (**a**) and axial pressure (**b**).

The maximum strain (MS) refers to the maximum value of the strain generated by the specimen after each impact under various axial and confining pressure conditions. The higher the MS, the greater the deformation of the specimen and the more severe the specimen damage. The variation law of MS with impact times is shown in Figure 14. The MS grows with increasing impact times under diverse P_a and P_c values. Due to the differences in P_c and P_a, the trend of the MS also changes, and the increasing trend lines appear to intersect or be approximately parallel. When P_a is constant, the MS decreases with increasing P_c values (Figure 14a), while when the P_c value is constant, the MS grows with increasing P_a values (Figure 14b). The changing trend in MS with impact times is exactly opposite to that of the DDM changing with impact times. When P_a = 8 MPa and the P_c values are 8 and 12 MPa, respectively, the trend lines of their MSs intersect, and a similar situation also occurs when P_c = 8 MPa and the P_a values are 14 and 20 MPa, respectively. In addition, when the P_c value is constant, the MS curve under a small P_a value appears in a slow growth stage with increasing impact times, since the deformation is relatively small during this stage due to compaction. Most samples experience a sudden increase in strain during the last one or several impacts, which is due to macroscopic rupture and a decrease in their ability to resist external loads.
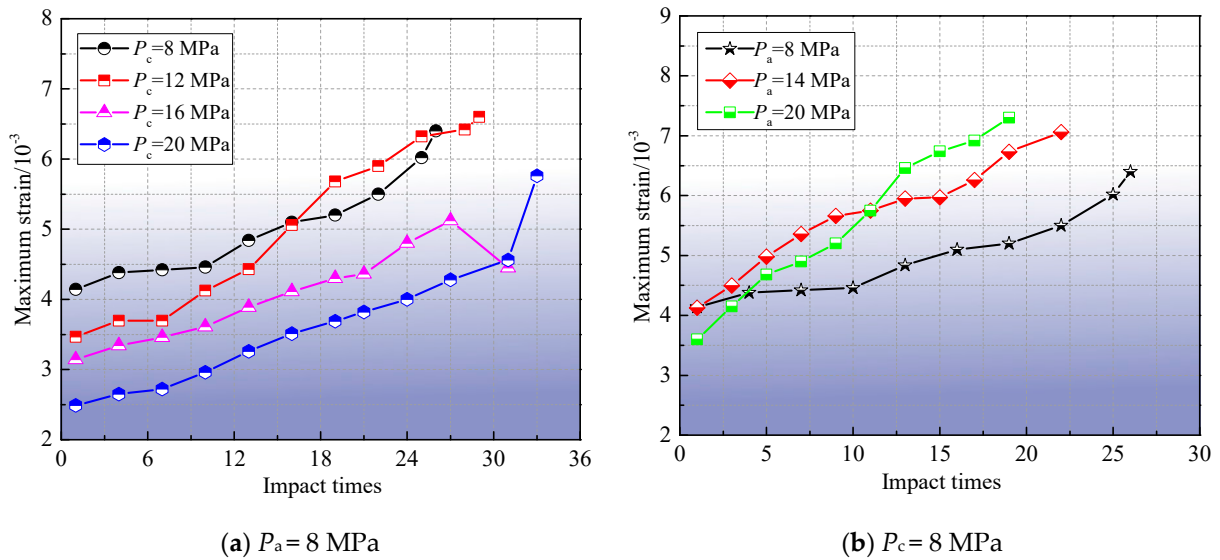
(a) $P_a = 8$ MPa   **(b)** $P_c = 8$ MPa

Figure 14. Variation in MS with impact times under different confining pressures (**a**) and axial pressures (**b**).

3.4.3. Impact Resistance Performance

Rock structure and stress conditions have a significant influence on the impact resistance of rocks. In repeated impact tests, the impact resistance of rocks is usually characterized by the number of impacts that they can withstand. To quantitatively analyze the correlation between the accumulated impact times (AITs) that rocks can withstand, confining pressure, and axial pressure, the correlation between the AIT and the ratio of P_c to P_a is plotted in Figure 15. As P_c/P_a grows, the AIT gradually rises, roughly showing a quadratic polynomial relationship. It can be predicted that as P_c/P_a further increases, the increased rate of AIT will gradually slow down. Because the pre-applied P_c limits the lateral deformation of the sample to a certain extent, there is no trend of crack propagation inside the specimen under axial pressure. The confining and axial pressures predominantly compact the original microcracks in the specimen, and the specimen eventually fails under repeated impact loads. With increasing impact times, the mechanical properties of the specimen deteriorate, and the effect of P_c and P_a on the sample failure can be gradually demonstrated. These findings can be used to accurately predict the total number of cyclic impacts that rocks can withstand under different confining and axial pressures, thus providing a basis for blasting parameter design and dynamic disaster prevention and control in rock engineering.
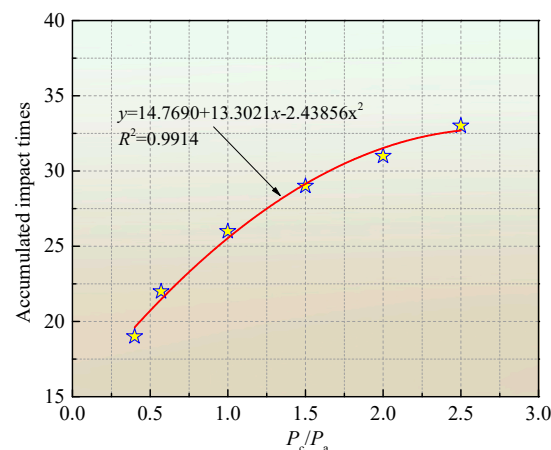

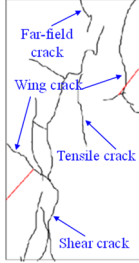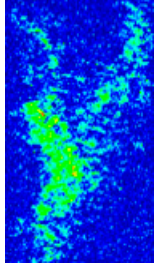**Figure 15.** Relationship between the AIT and P_c/P_a.
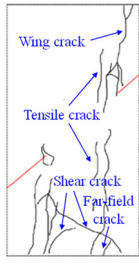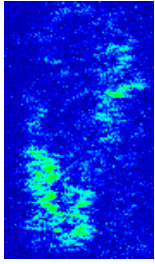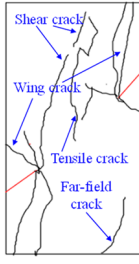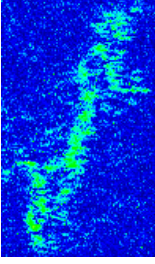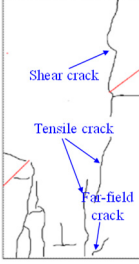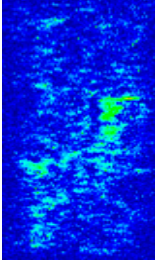
4. Dynamic Failure Mechanism

4.1. Fracture Behaviors

The fracture behavior of the specimen can be regarded as the result of the distribution and interaction between prefabricated fissures and original microcracks under impact loading. Analyzing the crack propagation morphology and fracture behavior of the fractured specimens is crucially important for understanding the fracturing and instability of rock masses under quasi-triaxial pressures and impact disturbance conditions. The fracture characteristics and corresponding sketches, as well as the NMRI results, of each specimen after the penultimate impact under diverse P_c and P_a values are listed in Table 2. After the penultimate impact, these specimens still have a certain degree of geometric integrity, which is conducive to observing the fracture characteristics of the specimens. Tensile cracks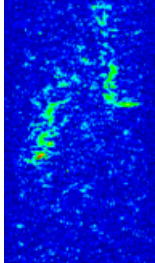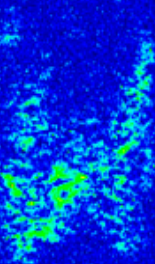 are identified as cracks propagating along the loading orientation, while shear cracks are considered as cracks propagating obliquely to the loading direction and forming visible shear bands [23,47]. As shown in Table 2, when P_a = 8 MPa, the number of cracks developed in the specimen tends to drop with increasing P_c values. In contrast, the cracks in sample FGS-1 are the most developed, while the cracks generated in sample FGS-4 are the least so, which can also be seen from their NMRI results. This is because the confining pressure improves the impact resistance of the specimen to a certain extent, and the greater the P_c value, the stronger the lateral constraint on the sample. In low confining pressure environments, the axial impact load induces both compressive and tensile stresses at the tips of prefabricated fissures and primary microcracks, forcing the specimen to undergo complex tensile and shear failure and resulting in an irregular final fracture surface. Under low P_c values (8, 12, and 16 MPa), numerous shear and tensile cracks arise in the samples, and these cracks are interconnected and converge to form large-scale macroscopic fracture surfaces, and the surface of the samples peels off, which will lead to a higher degree of ultimate destruction to the samples. In addition, due to brittle failure, abundant far-field cracks are generated in the samples. When the P_c is high, the initiation and expansion of microcracks in the sample are difficult. Repeated impact pressure promotes the specimen to develop approximately parallel to the crack end and gradually along the impact loading direction, resulting in a small angle between the fracture surface and the impact loading orientation. Some original microcracks in the specimen expand and penetrate, forming fewer macroscopic fracture surfaces, and the specimen does not undergo surface peeling, maintaining good integrity. The specimen under the higher P_c value (20 MPa) is mainly subjected to tensile failure, with localized small-scale shear failure.

On the other hand, axial pressure plays a key role in inducing cracks inside the specimen, thereby weakening the load-bearing capability of the microelements. When P_c = 8 MPa, with increasing P_a values, the compressive stress on the defective microstructure inside the sample increases, and the tendency of cracking in different directions increases, leading to different fracture behaviors. With multiple reflections and transmissions of stress waves, some shear cracks and tensile cracks emerge in the sample under the low P_a value (8 MPa). When the P_a is high, the microcracks inside the specimen undergo a small expansion after compaction, and repeated impacts induce the initiation of microcracks around the prefabricated fissures, promoting the accumulation of internal damage in the specimen. Under higher P_a values (14 and 20 MPa), anti-wing cracks and secondary coplanar cracks are developed in the specimens, mainly characterized by shear failure. Cracks perpendicular to the impact loading direction are generated in a local area of the sample, which may be caused by the sample breaking when expanding laterally.

Table 2. Fracture features of fractured specimens exposed to various axial and confining pressures and repeated impact loading.

Sample Number	Axial Pressure/MPa	Confining Pressure/MPa	Impact Times	Fracture Features	Sketches	Pore Distribution
FGS-1	8	8	25			
FGS-2	8	12	28			
FGS-3	8	16	30			
FGS-4	8	20	32			
FGS-5	14	8	21			
FGS-6	20	8	18			

Three types of cracks can be observed from the dynamic fracture characteristics of the samples exposed to various P_c and P_a values—tensile cracks, shear cracks, and tensile + shear cracks—which are determined by the behavior of crack initiation and expansion. The characteristic of tensile cracks is the opening of the crack surface, while the characteristic of shear cracks is the relative sliding along the crack surface. Tensile + shear cracks refer to cracks that start with one type of crack (tensile or shear) and then propagate with another type of crack. Tensile cracks generally begin at or near the tips of cracks or pores and propagate in a tortuous manner along the impact loading orientation. Their growth is initially stable but may become unstable during coalescence. The propagation path of these tensile cracks is not completely parallel to the impact loading direction but rather meanders through the specimen, which may be because the cracks always propagate along the boundaries of large mineral particles in the specimen matrix. Shear cracks generally propagate at a large angle to the impact loading direction, with both large-scale shear fracture surfaces and locally small-sized shear cracks, which depend on the compression conditions. The unstable process of shear crack propagation directly affects the fracture behavior of the specimen. Tensile + shear cracks are formed by the connection of tensile and shear cracks, and during their formation, both the micro-shear failure mechanism and micro-tensile failure mechanism exist in the sample. Generally, the growth of tensile + shear cracks is relatively stable in the early stage but may become unstable in the later stage. As the impact load is repeated, some secondary cracks emerge one after another, which are interconnected with the cracks produced earlier. The specimen is divided into multiple blocks, and the volume of the specimen expands laterally. After the penultimate impact, the growth lengths of these three types of cracks are limited and have not yet penetrated the entire specimen. In addition, by observing the fracture characteristics of all the specimens, it is found that for the initiation of microcracks, when the impact loading direction is in line with the original defect orientation around the tips of the prefabricated fissures, theoretically the microcracks should preferentially initiate at the stress concentration of the original flaws or the positions with the maximum tensile stress [7,48]. However, in practical situations, microcracks can also initiate at positions parallel to the impact loading direction without flaws. The presence of prefabricated fissures alters the stress distribution pattern in the specimen [49], and a high-stress concentration is easily formed around the fissures, leading to more cracks distributed around them. Note that the crack distribution in space is uneven, with some cracks expanding and closing, which is related to stress adjustment in the specimen. Furthermore, cracks do not propagate in two dimensions within a plane, but in three dimensions, and the internal crack propagation mode of the specimen is much more complex than the surface. The results of NMRI correspond well with the actual fracture morphology of the samples (Table 2).

4.2. Failure Modes

The fragmentation morphology of the samples after being impacted under different P_c and P_a values is shown in Figure 16. From Figure 16a–d, it can be seen that the fragmentation size of the broken specimen subjected to the same P_a value increases correspondingly with increasing P_c values, which is more evident after sample FGS-4 is broken. When the P_c value is smaller, the lateral constraint on the sample is insufficient, and the cracks in the specimen develop freely. With the increasing impact times, the degree of damage becomes more and more severe, which finally results in the macroscopic failure of the sample along the penetrated crack surface, forming a large number of fragments. When the P_c value is higher, it is more difficult to germinate new cracks in the specimen during impact. At this time, the impact pressure is not enough to promote the generation of considerable cracks in the specimen. Due to the small number of cracks generated during impact, the final

fracture surface formed is relatively small, resulting in a smaller number of fragmentations that ultimately fail the specimen and a corresponding larger fragmentation size. The results demonstrated that higher P_c values allowed fractured rocks to sustain greater loads and exhibit more ductile behavior. Hence, a certain range of confining pressure is proven to be an effective method of reducing rock brittleness and delaying rock failure.
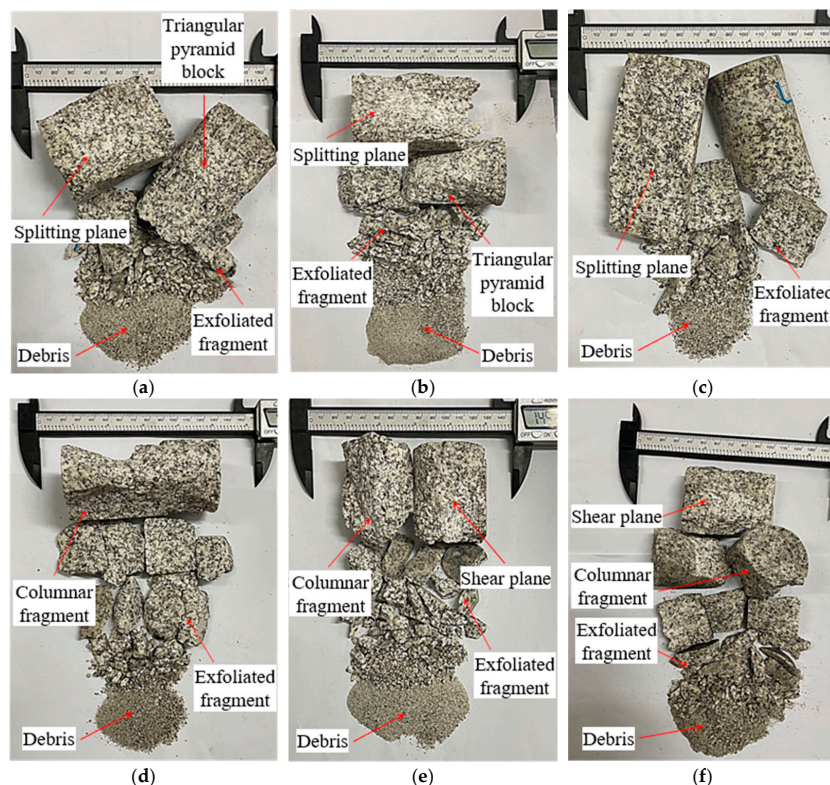

Figure 16. Failure modes of the fractured samples exposed to diverse quasi-triaxial pressures and repeated impact loading: (**a**) specimen FGS-1; (**b**) specimen FGS-2; (**c**) specimen FGS-3; (**d**) specimen FGS-4; (**e**) specimen FGS-5; (**f**) specimen FGS-6.

In Figure 16a,e,f, when the P_c value is the same, as the P_a rises, the fragmentation size of the fractured specimen tends to fall, which is more evident after the crushing of sample FGS-6. The same P_c value makes the specimen be subjected to the same lateral restraint. At this time, the greater the pre-applied P_a value, the more elastic energy is stored inside. When repeated impact disturbances induce the initiation of new cracks, due to the large amount of energy stored in the sample, the energy supply absorbed by crack initiation is sufficient, increasing the number of produced cracks. When the last impact occurs, the crack rapidly expands and penetrates, and the sample undergoes a phenomenon similar to a "rock burst", producing a large number of fragments.

When the P_c values are 8, 12, and 16 MPa (Figure 16a–c), some of the fragments have larger sizes and are shaped like splitting strips, and their fracture surfaces are relatively smooth with no noticeable friction marks, which implies that the failure pattern of these specimens is mainly tensile failure. Furthermore, the samples with P_c values of 8 and 12 MPa also produce small-scale triangular pyramid-shaped fragments, and their fracture surfaces are mostly oblique to the axis of the specimen and nearly penetrate through the entire specimen, indicating that these specimens also experience typical single-slope shear failure accompanied by tensile failure. In addition, when the P_a values are 14 and 20 MPa, the surface of the broken blocks of the specimens has obvious friction marks, and transgranular shear fracture occurs, accompanied by a large amount of rock debris. This suggests that these specimens experience intense friction between the blocks on both sides

of the fracture surfaces during the failure process, and the failure mode is mainly shear failure. Meanwhile, some fragments also have columnar shapes, indicating that these specimens undergo tensile failure simultaneously.

In summary, the instability and failure of rocks are the result of the combined action of static and dynamic loads. In particular, repeated impact loading accelerates the rock failure process, particularly in rocks with fissures. Progressive damage accumulation leads to a reduction in rock strength and subsequent rock failure over time. The interactions between the fissures, the surrounding rock matrix, and external forces lead to distinct deformation and failure patterns that are critical in rock engineering. Moreover, when the static load is within a certain range, the probability of disasters (such as rock bursts) occurring under dynamic disturbances is relatively high. That is, static pressures do not necessarily improve the rock's resistance to repeated impact loading, suggesting that there is an optimal pressure range for preventing failure. The loading history of the specimen shapes its internal crack distribution, thereby affecting its resistance to impact loads. The rock mass failure modes caused by dynamic loads can be summarized into two types: one is instability and failure dominated by dynamic loads, whose energy source predominantly originates from the dynamic loads; the other is instability and failure induced by dynamic loads, whose energy source predominantly comes from historical loads. This provides new ideas for understanding the mechanism of dynamic disasters in rock engineering and guiding future engineering design and disaster prevention.

5. Fractal Features

Recently, fractal theory has been widely applied as a nonlinear dynamic method. Under the combined action of pre-applied confining and axial pressures and repeated dynamic impact loads, fractured specimens gradually break up and produce fragments and debris with different sizes and masses. Currently, the distribution characteristics of these fragments and debris are usually analyzed from the aspects of fragment and debris size and mass to discuss the influence of confining and axial pressures on the fractal dimension of the fractured specimens. The fractal dimension of the sample directly and quantitatively reflects the degree of rock fragmentation. The greater the fractal dimension of the specimen and the more fragments and debris it contains, the higher the degree of fracture.

The fractal dimension of the specimen can be computed by the mass-equivalent side length of the fragments and debris:

$$D = 3 - \alpha \tag{5}$$

in which,

$$\alpha = \frac{lg\left(M_{L_{eq}}/M\right)}{lgL_{eq}} \tag{6}$$

where $M_{L_{eq}}$ is the debris mass corresponding to an equivalent edge length of L_{eq}; M is the total debris mass; D represents the fractal dimension of the debris; α means the slope value of $M_{L_{eq}}/M - L_{eq}$ in the double logarithmic coordinate system; and $M_{L_{eq}}/M$ represents the cumulative percentage content of the debris with an equivalent side length less than L_{eq}.

According to the calculation principles of fractal dimensions, the better the linear correlation between $lg\left(M_{L_{eq}}/M\right)$ and lgL_{eq} is, the more apparent the fractal characteristics of the fragments are. If the measured data exhibit a good linear correlation in several different segments, it indicates that the distribution has statistical self-similarity at multiple scales. The fractal dimension D, computed using Equations (5) and (6), ranges from 0 to 3. When $D = 0$–2, the larger-size fragments account for a significant proportion; when $D = 2$,

the mass proportions of fragments across different size ranges are equal; and when $D = 2–3$, the smaller-size fragments account for a larger proportion.

After repeated impact tests, the broken sample fragments and debris are collected and sieved. Due to the large amount of fine blocks and particles generated after sample crushing, the sample fragments are finely divided to facilitate the study of the features of the specimen fragments. Thus, the sieve sizes are 0–1, 1–2.5, 2.5–5, 5–10, 10–20, 20–35, 35–50, 50–75, and 75–100 mm, respectively. For fragments smaller than 5.0 mm, it is difficult to directly measure their size, so sieving is performed using a sieve with the corresponding aperture. For fragments larger than 5.0 mm, their size is first measured with a caliper, and then they are weighed. The mass of fragments in different size ranges is recorded, and the largest size fragment of each specimen is selected and weighed. The distribution of fragments after screening is shown in Figure 17.
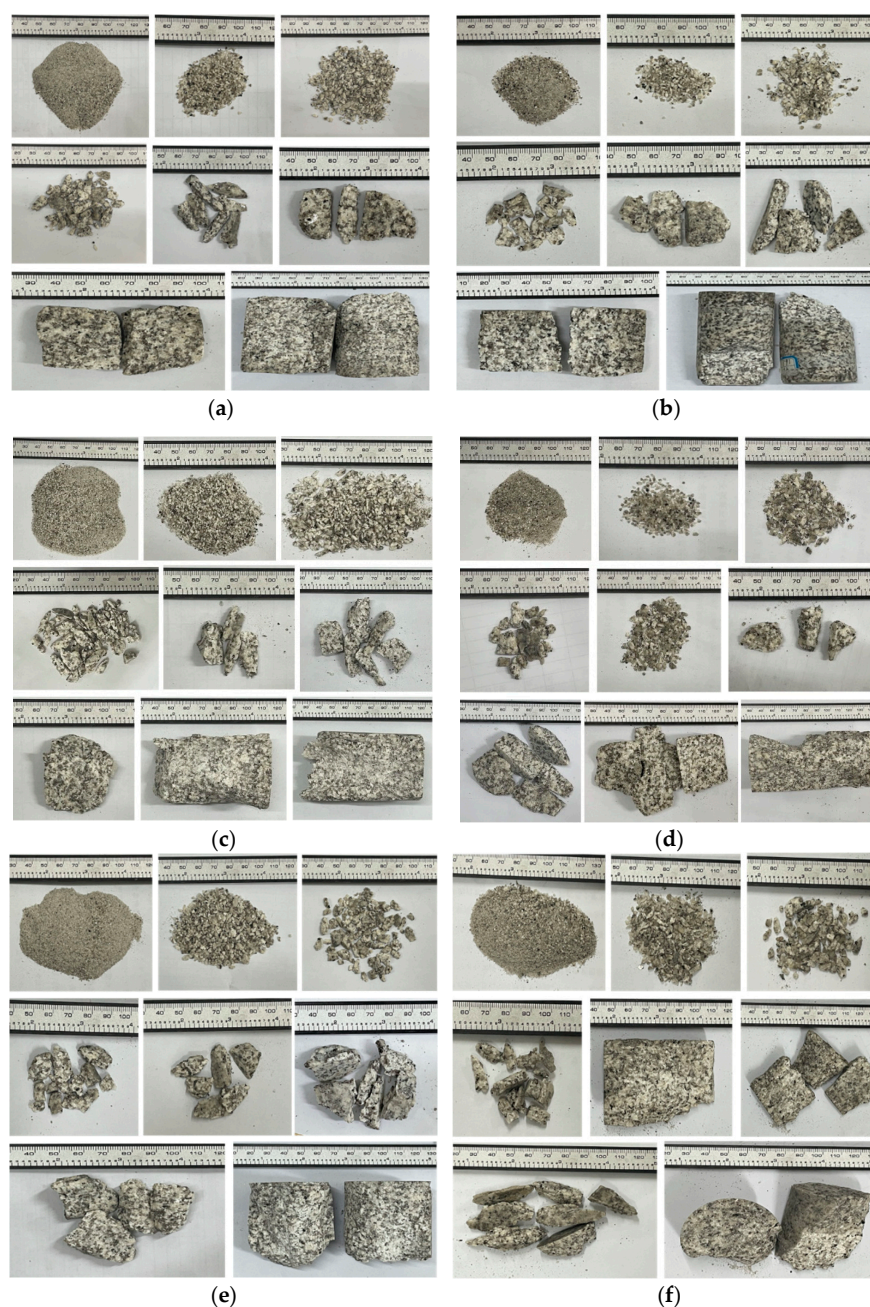

Figure 17. Distribution of sample fragments: (**a**) specimen FGS-1; (**b**) specimen FGS-2; (**c**) specimen FGS-3; (**d**) specimen FGS-4; (**e**) specimen FGS-5; (**f**) specimen FGS-6.

The sieving statistical results of the specimen fragments under different loading conditions are listed in Table 3, and the relationship between the equivalent edge length and the mass logarithm of the specimen fragments is presented in Figure 18. It can be found that there is a good linear correlation between $\lg\left(M_{L_{eq}}/M\right)$ and $\lg L_{eq}$, with correlation coefficients greater than 0.86, indicating that the fractal characteristics of the sample fragments under diverse loading conditions are very remarkable. The fractal dimension values of these specimens all lie between 2 and 3, indicating that the proportion of smaller-size fragments is relatively high, which is completely consistent with the actual situation. On the other hand, when P_a = 8 MPa and the P_c value increases gradually from 8 to 20 MPa, the fractal dimensions of the samples after repeated impacts are 2.44, 2.32, 2.23, and 2.12, respectively. This implies that as the P_c value grows, the fractal dimension shows a descending tendency. In other words, under the same P_a value, specimens that were pre-loaded with smaller P_c values will be more fragmented when subjected to the same impact load, and the degree of fragmentation of the specimens is less affected by the form of the impact load. This is because when the P_c value is small, the radial constraint on the specimen is relatively weak, allowing the more sufficient development and propagation of cracks inside the specimen under repeated impact disturbances, leading to larger cumulative damage and a higher degree of fragmentation of the sample. Whereas, when the P_c value is relatively large, the initial microcracks inside the specimen are compacted, and the specimen experiences greater radial constraint, resulting in an overall increase in specimen strength and making it less prone to severe fragmentation under the same repeated impact load.

Table 3. Statistics of sample fragment distribution.

Sample Number	Debris Mass/g									D
	0–1 mm	1–2.5 mm	2.5–5 mm	5–10 mm	10–20 mm	20–35 mm	35–50 mm	50–75 mm	75–100 mm	
FGS-1	15.91	4.98	11.93	18.48	19.92	20.73	105.94	297.17	/	2.44
FGS-2	6.40	2.14	3.67	7.84	16.0	38.03	121.98	/	308.36	2.32
FGS-3	16.02	5.68	11.86	12.14	6.42	21.81	26.24	156.34	245.07	2.23
FGS-4	5.80	1.15	5.37	4.68	9.06	10.74	39.27	95.21	336.77	2.12
FGS-5	18.95	10.61	9.32	10.24	22.08	58.53	100.89	/	251.56	2.46
FGS-6	24.00	15.88	12.96	17.33	36.18	66.27	190.75	136.69	/	2.52

In addition, when P_c = 8 MPa and the P_a values are 8, 14, and 20 MPa, the fractal dimensions of the samples obtained after repeated impacts are 2.44, 2.46, and 2.52, respectively. It can be observed that with increasing P_a values, the proportion of small-size fragments of the sample shows an increasing trend. Through the analysis of the failure mode and distribution characteristics of the fragments, it can be induced that the larger P_a values may have caused initial damage to the specimen structure. Under repeated impacts, numerous microcracks formed inside the specimen, which were previously subjected to the larger axial pressure, propagate and penetrate, releasing energy instantly, so that the specimen is severely damaged, and a large number of small-sized fragments are produced. Consequently, when the P_c value is constant, the higher the P_a value, the greater the fractal dimension and the higher the degree of fragmentation of the sample caused by the same repeated impacts. In this case, the risk of dynamic disasters occurring in the rock mass increases, and once a disaster occurs, it will cause significant harm.
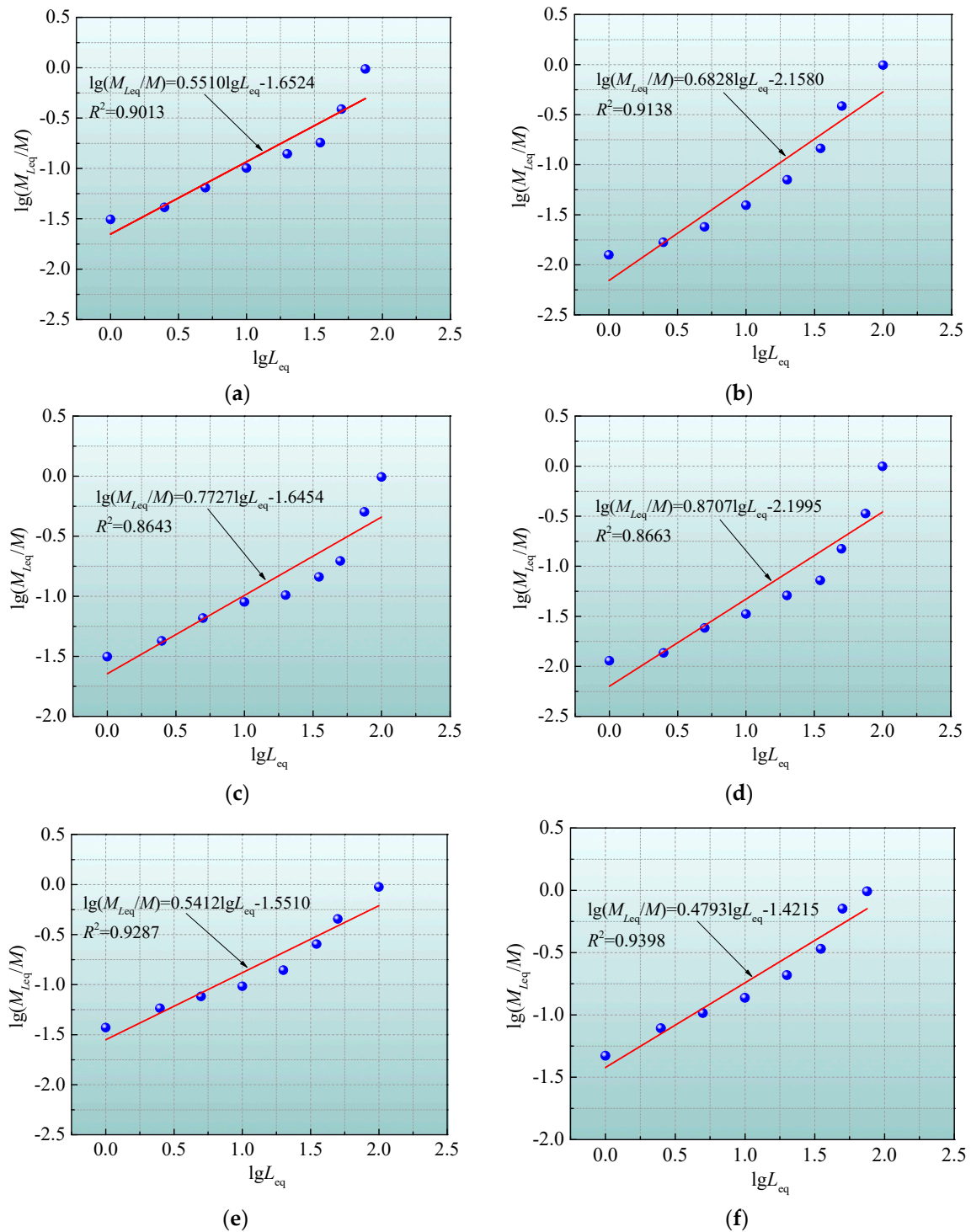
Figure 18. Equivalent side length–mass logarithm of specimen fragments: (**a**) specimen FGS-1; (**b**) specimen FGS-2; (**c**) specimen FGS-3; (**d**) specimen FGS-4; (**e**) specimen FGS-5; (**f**) specimen FGS-6.

By analyzing the fractal dimension of the fractured rock mass after failure under repeated impact loading, important guidance can be provided for rock engineering construction and disaster prevention and control, which is multifaceted. Fractured rock masses undergo multiple breakages and ruptures under repeated impact loads, eventually forming a certain group of fragments. The fractal dimension of the fragments can quantitatively describe their complexity and self-similarity. By analyzing the fractal dimension, the failure mode of the rocks exposed to dynamic loading can be predicted, allowing for an assessment of their stability and degree of failure. Moreover, studying the distribution characteristics of

the fragments can help engineers better understand the energy transfer, crack propagation, and fragmentation mechanisms of fractured rock masses in the fracture process, providing a more accurate mathematical model for rock mass failure analysis. Changes in the fractal dimension can be adopted to predict the extent of rock mass fragmentation and possible failure modes under different loading conditions. On the other hand, fractal dimension analysis can effectively evaluate the response characteristics of rock masses at different damage levels to disasters. Particularly under seismic or explosive loading, the extent of rock fragmentation is closely associated with the consequences of the disaster. Fragmented rock masses with high fractal dimensions may lead to changes in the spread features of seismic waves, increasing the risk of secondary disasters (such as landslides and collapses) after the main disaster. Thus, using the fractal dimension to assess fragment characteristics after rock mass failure can provide important data support for disaster prevention and control, emergency response, and safety management. Additionally, quantitative criteria for rock mass stability assessment can be provided by analyzing the fractal dimension. For example, during the construction of tunnels, mines, or other underground structures, the extent of damage to the rock mass under repeated impact loads may affect construction progress and safety risks. Fractal dimension analysis can help engineers design more reasonable support systems, predict any potential rock mass deformation and failure during different construction stages, and thus reduce risks during construction. Furthermore, more effective reinforcement measures are allowed to be taken, tailored to different rock mass failure modes.

6. Conclusions

(1) The amplitude of the transmitted wave declines with increasing axial pressure, the cracks develop in the specimen, and the damage progressively accumulates until the cracks propagate and penetrate. The amplitude of the transmitted wave descends with a rising P_c value, indicating that increasing the P_c value within a certain range can limit the initiation and growth of cracks in the sample, thereby enhancing the ability of the rock to resist external impacts. Moreover, the dynamic stress–strain curves of the samples exposed to diverse P_c and P_a values can be roughly divided into three stages: the approximate elastic stage, crack expansion stage, and post-failure stage, belonging to typical class II rebound curves. With increasing impact times, the strain rebound phenomenon gradually weakens. The difference in the dynamic stress–strain curves of the samples exposed to various P_c and P_a values is primarily manifested in the growth rate and plastic section.

(2) The impact times, P_a value, and P_c value all significantly affect mechanical properties. Under certain axial and confining pressures, with increasing impact times, the DPS and DDM of the specimen drop linearly, while the MS shows an opposite trend. When the P_a value is constant, with increasing P_c values the DPS, average DPS, DDM, and average DDM increase, while the MS declines. When the P_c value is constant, as the P_a value grows the DPS, average DPS, DDM, and average DDM appear to decrease, while the MS increases. In addition, as P_c/P_a rises, the AIT gradually increases, roughly showing a quadratic polynomial relationship.

(3) With multiple reflections and transmissions of stress waves, numerous shear cracks and tensile cracks developed in the specimens under low P_c values (8, 12, and 16 MPa), and these cracks are interconnected and converge to form large-scale macroscopic fracture surfaces, and the surface of the samples peels off, leading to a higher degree of ultimate destruction to the samples. The specimen under the higher P_c value (20 MPa) is mainly subjected to tensile failure, with localized small-scale shear failure. Moreover, some shear cracks and tensile cracks developed in the specimen under the low P_a value (8 MPa), while under the higher P_a values (14 and 20 MPa), anti-wing cracks and secondary coplanar

cracks developed in the specimens, mainly characterized by shear failure. Overall, three types of cracks can be observed from the dynamic fracture characteristics of the samples exposed to various P_c and P_a values—tensile cracks, shear cracks, and tensile + shear cracks—which are determined by the behavior of crack initiation and propagation.

(4) When P_a = 8 MPa and the P_c value increases gradually from 8 to 20 MPa, the fractal dimensions of the samples after repeated impacts are 2.44, 2.32, 2.23, and 2.12, respectively. This implies that as the P_c value rises, the fractal dimension shows a downward tendency. In addition, when P_c = 8 MPa and the P_a values are 8, 14, and 20 MPa, the fractal dimensions of the samples obtained after repeated impacts are 2.44, 2.46, and 2.52, respectively. The larger the pre-applied axial pressure, the greater the fractal dimension and the higher the degree of fragmentation of the sample caused by the same repeated impacts. By analyzing the fractal dimension of the fractured rocks after failure under repeated impact loading, important guidance can be provided for rock engineering construction and disaster prevention and control.

Author Contributions: Conceptualization, P.L. and J.Z.; methodology, J.Z.; software, Y.L. and Z.D.; validation, P.L., Y.L. and J.Z.; formal analysis, P.L., Y.L. and J.Z.; investigation, J.Z.; resources, P.L. and J.Z.; data curation, X.W.; writing—original draft preparation, P.L. and J.Z.; writing—review and editing, J.Z.; visualization, Z.D. and X.W.; supervision, S.M. and M.C.; project administration, J.Z.; funding acquisition, P.L., M.C. and S.M. All authors have read and agreed to the published version of the manuscript.

Data Availability Statement: The original contributions presented in this study are included in the article.

Conflicts of Interest: Author Jie Zhang was employed by the company China ENFI Engineering Corporation. The remaining authors declare that the research was conducted in the absence of any commercial or financial relationships that could be construed as a potential conflict of interest.

References

1. Naderloo, M.; Moosavi, M.; Ahmadi, M. Using acoustic emission technique to monitor damage progress around joints in brittle materials. *Theor. Appl. Fract. Mech.* **2019**, *104*, 102368. [CrossRef]

2. Wang, Y.; Song, Z.Y.; Mao, T.Q.; Zhu, C. Macro–meso fracture and instability behaviors of hollow-cylinder granite containing fissures subjected to freeze–thaw–fatigue loads. *Rock Mech. Rock Eng.* **2022**, *55*, 4051–4071. [CrossRef]

3. Li, P.; Cai, M.F.; Guo, Q.F.; Ren, F.H. Investigation on acoustic emission characteristics of hole-joint contained granite under a compressive disturbance: Experimental insights. *Lithosphere* **2022**, *2022*, 3594940. [CrossRef]

4. Sagong, M.; Park, D.; Yoo, J.; Lee, J.S. Experimental and numerical analyses of an opening in a jointed rock mass under biaxial compression. *Int. J. Rock Mech. Min. Sci.* **2011**, *48*, 1055–1067. [CrossRef]

5. Afolagboye, L.O.; He, J.M.; Wang, S.J. Crack initiation and coalescence behavior of two non-parallel flaws. *Geotech. Geol. Eng.* **2018**, *36*, 105–133. [CrossRef]

6. Park, C.H.; Bobet, A. Crack initiation, propagation and coalescence from frictional flaws in uniaxial compression. *Eng. Fract. Mech.* **2010**, *77*, 2727–2748. [CrossRef]

7. Li, P.; Cai, M.F.; Gao, Y.B.; Wang, P.T.; Miao, S.J.; Wang, Y. Fracture evolution and failure behavior around an opening in brittle jointed rocks subjected to uniaxial compression. *Theor. Appl. Fract. Mech.* **2022**, *122*, 103651. [CrossRef]

8. Li, P.; Wu, Y.Q.; Cai, M.F. Failure behavior of the surrounding rock of jointed rock masses in a gold mine under blasting impact disturbance. *Environ. Earth Sci.* **2022**, *81*, 106. [CrossRef]

9. Li, P.; Cai, M.F.; Gao, Y.B.; Gorjian, M.; Miao, S.J.; Wang, Y. Macro/mesofracture and instability behaviors of jointed rocks containing a cavity under uniaxial compression using AE and DIC techniques. *Theor. Appl. Fract. Mech.* **2022**, *122*, 103620. [CrossRef]

10. Resende, R.; Lamas, L.N.; Lemos, J.V.; Calçada, R. Micromechanical modelling of stress waves in rock and rock fractures. *Rock Mech. Rock Eng.* **2010**, *43*, 741–761. [CrossRef]

11. Li, X.B.; Li, C.J.; Cao, W.Z.; Tao, M. Dynamic stress concentration and energy evolution of deep-buried tunnels under blasting loads. *Int. J. Rock Mech. Min. Sci.* **2018**, *104*, 131–146. [CrossRef]

12. Li, P.; Cai, M.F.; Gao, Y.B.; Wang, P.T.; Miao, S.J.; Wang, Y.; Xi, X. Dynamic mechanical behavior and cracking mechanism of cross-jointed granite containing a hole. *J. Mater. Res. Technol.* **2023**, *22*, 1572–1594. [CrossRef]

13. Li, P.; Cai, M.F.; Miao, S.J.; Li, Y.; Wang, Y. Correlation between the rock mass properties and maximum horizontal stress: A case study of overcoring stress measurements. *Int. J. Miner. Metall. Mater.* **2025**, *32*, 39–48. [CrossRef]

14. Feng, F.; Li, X.B.; Luo, L.; Zhao, X.D.; Chen, S.J.; Jiang, N.; Huang, W.P.; Wang, Y.J. Rockburst response in hard rock owing to excavation unloading of twin tunnels at great depth. *Bull. Eng. Geol. Environ.* **2021**, *80*, 7613–7631. [CrossRef]

15. Li, P.; Cai, M.F.; Miao, S.J.; Ren, F.H.; Gorjian, M.; Peng, C. Mechanism, prevention, and control of mining-induced dynamic disasters in underground metal mines in China: Challenges and solutions. *J. Cent. South Univ.* **2024**, *31*, 2549–2606. [CrossRef]

16. Dai, L.P.; Pan, Y.S.; Xiao, Y.H.; Wang, A.W.; Wang, W.; Wei, C.C.; Fan, D.W. Parameter design method for destressing boreholes to mitigate roadway coal bursts: Theory and verification. *Rock Mech. Rock Eng.* **2024**, *57*, 9539–9556. [CrossRef]

17. Dai, L.P.; Pan, Y.S.; Zhang, C.G.; Wang, A.W.; Canbulat, I.; Shi, T.W.; Wei, C.C.; Cai, R.H.; Liu, F.Y.; Gao, X.P. New criterion of critical mining stress index for risk evaluation of roadway rockburst. *Rock Mech. Rock Eng.* **2022**, *55*, 4783–4799. [CrossRef]

18. Zhao, J.; Zhao, X.B.; Cai, J.G. A further study of P-wave attenuation across parallel fractures with linear deformational behaviour. *Int. J. Rock Mech. Min. Sci.* **2006**, *43*, 776–788. [CrossRef]

19. Li, X.B.; Zhou, T.; Li, D.Y. Dynamic strength and fracturing behavior of single-flawed prismatic marble specimens under impact loading with a split-Hopkinson pressure bar. *Rock Mech. Rock Eng.* **2017**, *50*, 29–44. [CrossRef]

20. Wang, Y.B.; Zhou, X.Y.; Kong, J.; Yu, B.B. Dynamic fracture experiment of fractured rock under dynamic loading. *Shock Vib.* **2020**, *2020*, 9761650. [CrossRef]

21. You, W.; Dai, F.; Liu, Y.; Li, Y.Z. Dynamic mechanical responses and failure characteristics of fractured rocks with hydrostatic confining pressures: An experimental study. *Theor. Appl. Fract. Mech.* **2022**, *122*, 103570. [CrossRef]

22. Shi, H.; Chen, W.L.; Zhang, H.Q.; Song, L.; Li, M.; Wang, M.J.; Lu, P.J. Dynamic strength characteristics of fractured rock mass. *Eng. Fract. Mech.* **2023**, *292*, 109678. [CrossRef]

23. Li, P.; Cai, M.F.; Gao, Y.B.; Guo, Q.F.; Miao, S.J.; Ren, F.H.; Wang, Y. Mechanical responses and fracturing behavior of jointed rock masses with a cavity under different dynamic loads. *Int. J. Impact Eng.* **2023**, *178*, 104608. [CrossRef]

24. Qiu, J.D.; Zhou, C.T.; Wang, Z.H.; Feng, F. Dynamic responses and failure behavior of jointed rock masses considering pre-existing joints using a hybrid BPM-DFN approach. *Comput. Geotech.* **2023**, *155*, 105237. [CrossRef]

25. Chen, Y.; Yu, D.F.; Wang, Y.X.; Zhao, Y.L.; Yang, H.W.; Huang, L.C. Dynamic characteristics and anchorage mechanisms of fractured granite: Analytical, numerical and experimental analyses. *Rock Mech. Rock Eng.* **2024**. [CrossRef]

26. Jiang, Z.; Deng, H.W.; Liu, T.Y.; Tian, G.L.; Tang, L.H. Study on microstructural evolution of marble under cyclic dynamic impact based on NMR. *IEEE Access* **2019**, *7*, 138043–138055. [CrossRef]

27. Wang, P.; Yin, T.B.; Li, X.B.; Zhang, S.S.; Bai, L. Dynamic properties of thermally treated granite subjected to cyclic impact loading. *Rock Mech. Rock Eng.* **2019**, *52*, 991–1010. [CrossRef]

28. Jiang, Z.; Yu, S.T.; Deng, H.W.; Deng, J.R.; Zhou, K.P. Investigation on microstructure and damage of sandstone under cyclic dynamic impact. *IEEE Access* **2019**, *7*, 133145–133158. [CrossRef]

29. Lu, H.; Chen, Q.L.; Ma, X.T. Investigation into dynamic behaviors of high-temperature sandstone under cyclic impact loading using DIC technology. *Appl. Sci.* **2022**, *12*, 9247. [CrossRef]

30. Wang, X.S.; Guo, L.J.; Xu, Z.Y.; Liu, X.; Xu, J.L.; Pan, B.; Deng, D. Dynamic response and damage evolution of red sandstone with confining pressure under cyclic impact loading. *Fatigue Fract. Eng. Mater. Struct.* **2023**, *46*, 1078–1092. [CrossRef]

31. Xue, J.C.; Zhao, Z.Y.; Dong, L.J.; Jin, J.F.; Zhang, Y.B.; Tan, L.; Cai, R.Y.; Zhang, Y.H. Effect of chemical corrosion and axial compression on the dynamic strength degradation characteristics of white sandstone under cyclic impact. *Minerals* **2022**, *12*, 429. [CrossRef]

32. Zhang, J.; Xi, X.; Tan, W.H.; Wu, X.; Wu, X.H.; Guo, Q.F.; Cai, M.F. Experimental investigation of failure mechanisms of granites with prefabricated cracks induced by cyclic-impact disturbances. *Energies* **2022**, *15*, 3680. [CrossRef]

33. Luo, N.; Suo, Y.C.; Zhang, H.H.; Chai, Y.B.; Zhai, C.; Qu, Z.; Bai, G.Z. On dynamic behaviors and failure of bedding coal rock subjected to cyclic impact. *Explos. Shock Waves* **2023**, *43*, 42–55.

34. Liu, X.R.; Yang, S.Q.; Huang, Y.H.; Cheng, J.L. Experimental study on the strength and fracture mechanism of sandstone containing elliptical holes and fissures under uniaxial compression. *Eng. Fract. Mech.* **2019**, *205*, 205–217. [CrossRef]

35. Li, X.B.; Lok, T.S.; Zhao, J.; Zhao, P.J. Oscillation elimination in the Hopkinson bar apparatus and resultant complete dynamic stress–strain curves for rocks. *Int. J. Rock Mech. Min. Sci.* **2000**, *37*, 1055–1060. [CrossRef]

36. Kolsky, H. An investigation of the mechanical properties of materials at very high rates of loading. *Proc. Phys. Soc. Sect. B* **1949**, *62*, 676–700. [CrossRef]

37. Zhou, Z.; Tan, L.; Cao, W. Fracture evolution and failure behaviour of marble specimens containing rectangular cavities under uniaxial loading. *Eng. Fract. Mech.* **2017**, *184*, 183–201. [CrossRef]

38. Li, B.Q.; Einstein, H.H. Comparison of visual and acoustic emission observations in a four point bending experiment on barre granite. *Rock Mech. Rock Eng.* **2017**, *50*, 2277–2296. [CrossRef]

39. Ravichandran, G.; Subhash, G. Critical appraisal of limiting strain rates for compression testing of ceramics in a split hopkinson pressure bar. *J. Am. Ceram. Soc.* **1994**, *77*, 263–267. [CrossRef]

40. Weng, L.; Li, X.B.; Shang, X.Y.; Xie, X.F. Fracturing behavior and failure in hollowed granite rock with static compression and coupled static–dynamic loads. *Int. J. Geomech.* **2018**, *18*, 4018045. [CrossRef]

41. Tao, M.; Ma, A.; Cao, W.Z.; Li, X.B.; Gong, F.Q. Dynamic response of pre-stressed rock with a circular cavity subject to transient loading. *Int. J. Rock Mech. Min. Sci.* **2017**, *99*, 1–8. [CrossRef]

42. Zou, C.J.; Wong, L.N.Y.; Loo, J.J.; Gan, B.S. Different mechanical and cracking behaviors of single-flawed brittle gypsum specimens under dynamic and quasi-static loadings. *Eng. Geol.* **2016**, *201*, 71–84. [CrossRef]

43. Zhu, Q.Q.; Li, D.Y.; Han, Z.Y.; Xiao, P.; Li, B. Failure characteristics of brittle rock containing two rectangular holes under uniaxial compression and coupled static-dynamic loads. *Acta Geotech.* **2022**, *17*, 131–152. [CrossRef]

44. Su, Q.Q.; Ma, Q.Y.; Ma, D.D.; Yuan, P. Dynamic mechanical characteristic and fracture evolution mechanism of deep roadway sandstone containing weakly filled joints with various angles. *Int. J. Rock Mech. Min. Sci.* **2021**, *137*, 104552. [CrossRef]

45. Zhan, J.W.; Zhou, Y.L.; Wang, Y.; Huang, M.; Jiang, S. Experimental study on physical damage and mechanical degradation of granite subjected to high-temperature cooling impact cycling. *Rock Soil Mech.* **2024**, *45*, 2362–2372.

46. Tang, L.Z.; Wang, C.; Cheng, L.P.; Gao, L.H. Experimental study of mechanical characteristics of skarn under one-dimensional coupled static and cyclic impact loads. *J. Cent. South Univ. (Sci. Technol.)* **2015**, *46*, 3898–3906.

47. Weng, L.; Wu, Z.J.; Li, X.B. Mesodamage characteristics of rock with a pre-cut opening under combined static–dynamic loads: A nuclear magnetic resonance (NMR) investigation. *Rock Mech. Rock Eng.* **2018**, *51*, 2339–2354. [CrossRef]

48. Zou, C.; Wong, L.N.Y. Experimental studies on cracking processes and failure in marble under dynamic loading. *Eng. Geol.* **2014**, *173*, 19–31. [CrossRef]

49. Wong, L.N.Y.; Zhang, X.P. Size effects on cracking behavior of flaw-containing specimens under compressive loading. *Rock Mech. Rock Eng.* **2014**, *47*, 1921–1930. [CrossRef]